







State-resolved differential cross sections of single-electron capture in swift collisions of $C^{4+}(1s2s^3S)$ ions with gas targets

I. Madesis ^{1,2}, A. Laoutaris ^{1,2}, S. Nanos ^{2,3}, S. Passalidis ⁴, A. Dubois,⁴ T. J. M. Zouros ^{1,2} and E. P. Benis ^{3,*}

¹Department of Physics, University of Crete, GR-70013 Heraklion, Greece

²Tandem Accelerator Laboratory, Institute of Nuclear and Particle Physics, NCSR “Demokritos”, GR-15310 Ag. Paraskevi, Greece

³Department of Physics, University of Ioannina, GR-45110 Ioannina, Greece

⁴Sorbonne Université, CNRS, Laboratoire de Chimie Physique-Matière et Rayonnement, F-75005 Paris, France



(Received 19 March 2022; accepted 31 May 2022; published 15 June 2022)

We report on double and single differential cross section measurements of the $1s2s^2\ ^2S$, $1s2s2p\ ^2P_{\pm}$, and $1s2s2p\ ^4P$ doubly excited states produced by single-electron capture in 6–15 MeV collisions of pre-excited $C^{4+}(1s2s^3S)$ ions with H_2 , He, Ne, and Ar targets. *Ab initio* cross section calculations based on a three active electrons atomic orbital close-coupling approach are compared to the measurements for collisions with the lighter H_2 and He targets, showing an overall good agreement. Theoretical details concerning Auger electron angular distributions, partial cross sections, impact parameter dependencies, and radiative cascade feeding effects are discussed. The populations of the $1s2s2p\ ^4P$, $^2P_{-}$, $^2P_{+}$ multiplets concerning the spin symmetry are finally presented for the four collision systems and discussed following the comparisons between theory and experiment.

DOI: [10.1103/PhysRevA.105.062810](https://doi.org/10.1103/PhysRevA.105.062810)

I. INTRODUCTION

The fundamental process of single-electron capture (SEC) in ion-atom collisions and the related dynamics of a many-body quantum system is a challenging theoretical problem. Even for the simple system of proton scattering from a hydrogen atom, richly studied both theoretically and experimentally, its theoretical description and modeling are still under investigation (see Ref. [1] and references therein). Modern theoretical SEC treatments are oriented towards semiclassical close-coupling approaches (e.g., atomic orbital close-coupling (AOCC) [1–3], two-center basis generator method (TC-BGM) [4,5], molecular orbital close-coupling (MOCC) [6]), as well as lattice-based finite-difference calculations [7], classical trajectory Monte Carlo (CTMC) simulations [8], continuum distorted-wave (CDW) approaches at sufficiently high incident energies [9], and other perturbative methods. Although numerous SEC experimental results have been reported since the advent of accelerators in an effort to model total cross section dependencies [10], only state-selective SEC studies have offered the most stringent tests of theory. State-selective SEC data obtained with the techniques of energy gain spectroscopy [11,12], x-ray spectroscopy [13,14], Auger spectroscopy [15–18], and COLTRIMS [4,19–24] have been reported during the last decades. The results of these studies, aside from their inherent physical significance towards the detailed understanding and modeling of the SEC process, are essential for the development of a number of fields such as astrophysics [25,26] and plasma physics [27].

Despite the abundance of state-selective SEC studies, only recently has SEC involving multi-open-shell excited ions received attention [5,15–18,28]. This is a demanding theoretical

problem, as it is of multielectron nature and inherently bears important dynamic electron correlation effects. Furthermore, it offers the testing grounds for examining the validity of the commonly used single active electron picture, adopted in independent electron, independent event, and frozen core approximations, as well as arguments concerning the population of levels following spin statistics [16–18,28,29]. It should be pointed out that the SEC of a target electron to the ground state of an ion primarily results in *singly* excited states that can be explored by time-of-flight techniques [30] and various photonic deexcitation spectroscopies [14,31]. Alternatively, SEC to excited ionic states (e.g., $1s2s^3S$ for He-like ions) may give rise to *doubly* excited states much more efficiently explored by state-resolved Auger spectroscopy, particularly for low- Z_p ions [15].

Recently, the long-standing problem of how a multi-unpaired-electron ion core behaves while undergoing SEC during fast ion-atom collisions has been resolved [28]. There, focusing on swift collisions of $C^{4+}(1s2s^3S)$ ions with helium and dihydrogen, we presented results on the formation of doubly excited $C^{3+}(1s2s2p)\ ^4P$ and $^2P_{\pm}$ states, where $^2P_{-}$ and $^2P_{+}$ correspond to the doublet levels of lowest and highest energies, respectively. Emphasis was primarily given to the ratio R of the $^4P / ^2P_{\pm}$ SEC cross sections as a measure of the spin statistics population ratio. High statistics state-resolved KLL Auger spectra, strongly supported by intensive close-coupling calculations involving the dynamics of three active electrons (3eAOCC), highlighted the importance of strong electron correlations. At the same time, these results also exposed the weaknesses of both statistical arguments and single active electron approximations in modeling the populations of the atomic states originating from capture.

This paper is an extension of our work already presented in Ref. [28]. Here we are concerned with the detailed study of the SEC process induced in collisions between $C^{4+}(1s2s^3S)$

*Corresponding author: mbenis@uoi.gr

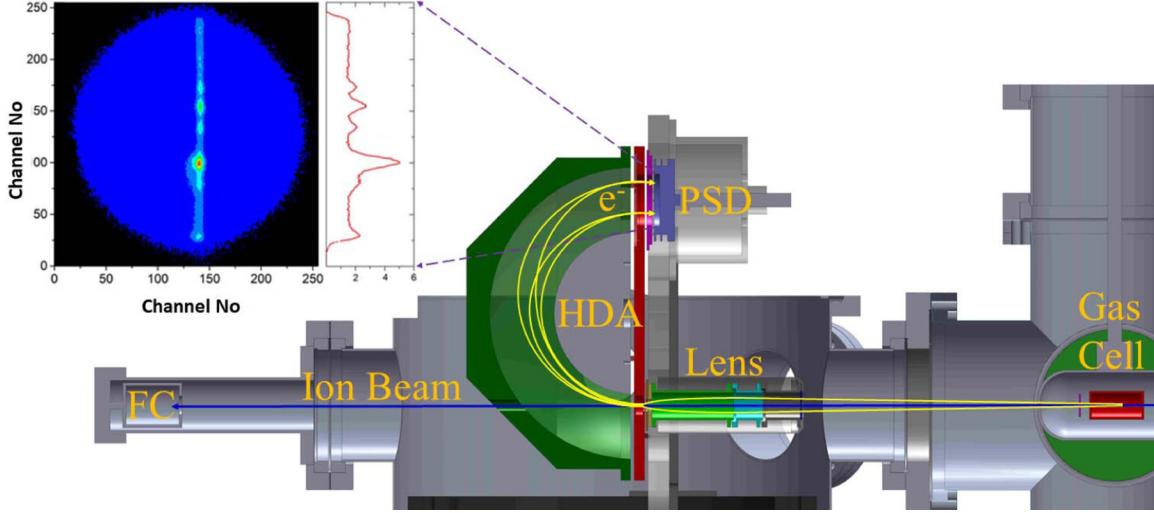
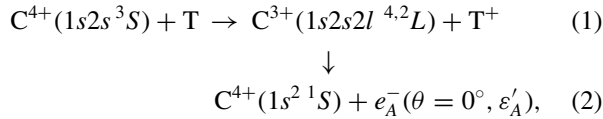


FIG. 1. Cross-sectional view of our ZAPS experimental setup. Electrons emitted at $\theta = 0^\circ$ with respect to the ion beam direction are first decelerated and focused onto the entry of the HDA by the injection lens and subsequently energetically analyzed by the HDA and imaged onto the 2D PSD within a narrow strip along the dispersion axis (as seen in the inset). The projection of the image along the dispersion axis corresponds to the electron spectrum in red shown in the inset.

projectiles and different gas targets (T: H₂, He, Ne, Ar), i.e.,



where θ is the electron observation angle with respect to the projectile beam direction and ε'_A the Auger electron energy in the rest frame of the projectile. Double and single differential cross sections (DDCS and SDCS, respectively) are reported for the production of the $1s2s^2\ ^2S$, $1s2s2p\ ^2P_{\pm}$, and $1s2s2p\ ^4P$ states. 3eAOCC calculations are detailed and compared to the measurements on the SDCS level. Additional information with respect to the angular distributions, the partial cross section contributions, and the process probability dependence on the impact parameter is provided. Finally, further support of the nonstatistical population of the above states is also given.

II. EXPERIMENT

A. The experimental setup

High-resolution KLL Auger electron spectra were obtained using the zero-degree Auger projectile spectroscopy (ZAPS) [32] experimental station located at the NCSR “Demokritos” 5.5 MV Tandem accelerator facility [33]. This ZAPS setup, illustrated in Fig. 1, has been described in detail in Refs. [34,35]. The electron spectrometer consists of an electrostatic single-stage hemispherical deflector analyzer (HDA) equipped with a four-element injection lens and a two-dimensional position sensitive detector (2D PSD). The C⁴⁺ ion beam passes through the doubly differentially pumped gas cell, where it interacts with the gas target, and upon exiting continues on through the spectrometer to be collected in a Faraday cup for normalization purposes. KLL Auger electrons generated from the deexcitation of the C³⁺(1s2l2l') electronic configurations [Eq. (2)], produced in the collision and emitted

in the forward direction along the ion beam ($\theta = 0^\circ$), are preretarded and focused by the injection lens onto the entry of the HDA to improve their energy resolution and collection efficiency. They are then energetically analyzed by the HDA and imaged onto the 2D PSD within a narrow strip along the dispersion axis [36]. The projection of the image onto the dispersion axis results in the Auger electron spectrum, as shown in the inset of Fig. 1. In this study, high statistics spectra were recorded with sufficient energy resolution (0.15%) to clearly separate the C³⁺(1s2l2l') KLL Auger lines.

B. Electron yield normalization

In ZAPS, the measured electron DDCS is determined from the following formula [32,37]:

$$DDCS_j \equiv \frac{d^2\sigma_j}{d\Omega dE_j} = \frac{N_j^e}{N_l L_{\text{eff}} n \overline{\Delta\Omega} \Delta E_j T \eta}, \quad (3)$$

where N_j^e is the number of electrons detected in channel j (out of a 256 channels binning scheme used on the PSD), L_{eff} the effective length of the target gas cell, N_l the number of ions collected in the Faraday cup, n the target gas density, $\overline{\Delta\Omega}$ the effective solid angle averaged over the length of the gas cell, ΔE_j the energy step per channel in the spectrum, and T the analyzer transmission determined here by three electroformed meshes of 90% transmission each. The absolute overall spectrograph efficiency η was obtained by performing auxiliary *in situ* measurements of either elastically scattered (binary encounter) electrons from bare C⁶⁺ ion beams, as typically done for increased accuracy in all such ZAPS measurements [32,38], and/or measurements of the target Ne-KLL Auger production utilizing proton beams [32,39]. Both methods gave very similar results, i.e., an overall efficiency $\eta = (50 \pm 5)\%$. It should be noted that our present data acquisition system allows for a maximum count rate of about 100 kHz with negligible dead time. The DDCS are then transformed to the projectile rest frame according to the kinematics

transformation [32]:

$$\frac{d^2\sigma}{d\Omega'd\varepsilon'} = \frac{d^2\sigma}{d\Omega d\varepsilon} \sqrt{\frac{\varepsilon'}{\varepsilon}}, \quad (4)$$

where the quantities in the projectile rest frame are denoted with primed symbols. The electron kinetic energy ε' in the projectile rest frame can be related to the corresponding laboratory frame kinetic energy ε as [32]

$$\varepsilon'(t_p, \varepsilon) = \varepsilon + t_p - 2 \cos \theta \sqrt{\varepsilon t_p}, \quad (5)$$

with

$$t_p = \frac{m}{M_p} E_p = 548.58 \frac{E_p (\text{MeV})}{M_p (\text{u})} (\text{eV}) \quad (6)$$

being the reduced projectile energy known also as the *cusp* electron energy (electrons isotactic to the projectile ion). θ is the angle between the vectors of the projectile velocity \mathbf{V}_p and the emitted Auger electron velocity in the laboratory frame \mathbf{v} , with $\theta = 0^\circ$ in our ZAPS measurements. E_p and M_p are the kinetic energy and mass of the projectile, respectively, while m is the electron mass.

C. Mixed-state He-like ion beams

Our experiments necessitate the use of He-like ion beams pre-excited in the $1s2s\ ^3S$ state. However, He-like ion beams produced in tandem Van de Graaff accelerators are typically delivered in a mixture of $1s^2\ ^1S$ ground and $1s2s\ ^{1,3}S$ metastable states [40]. The $1s2s\ ^1S$ component has a reduced production probability, i.e., 1/3 of that for the $1s2s\ ^3S$, assuming a statistical production probability. Moreover, due to its lifetime of $3\ \mu\text{s}$ (much shorter than the lifetime of 20 ms of the $1s2s\ ^3S$ component [40]) it suffers further population reduction up to the target area. Depending on the production method and location (12.1 m or 26.4 m from the target) this value may be further reduced from 25% to 50% [40]. In addition, the contribution of the $1s2s\ ^1S$ component to the formation of the $1s2s2p\ ^4P$ state is negligible (spin forbidden), while the contribution to the $1s2s2p\ ^2P$ states was found to be marginal upon calculation. Thus, hereafter, its contribution to the analysis of the data will be omitted. To extract the contributions of the ground state from those of the metastable state component we use our recently reported mixed-state beam method [41]. It relies on varying the metastable fraction in the He-like ion beams, which is possible by utilizing different stripping media, i.e., gas or foil. In the case of gas stripping, the metastable fraction depends also on the stripping energy [42,43], while in the case of foil stripping it depends mostly on the atomic number and thickness of the foil [42,44–48]. Our method requires performing two different measurements with He-like beams of appreciably different $1s2s\ ^3S$ metastable content as expressed by the relative intensities of the $1s2s2p\ ^4P$ peak [35,40,41]. The first measurement utilizes a high metastable fraction typically obtained with carbon foil stripping, either inside the accelerator tank at the terminal (foil terminal stripping, FTS) or at a post-stripper after the accelerator tank (foil poststripping, FPS). The choice of FTS or FPS method depends mostly on the ion beam energy. The second measurement utilizes a lower metastable fraction typically obtained with N_2 gas stripping

either inside the accelerator tank (gas terminal stripping, GTS) or outside the accelerator tank (gas poststripping, GPS). Thus, we utilized two different stripper positions: one inside the terminal, at a distance of ~ 26.4 m, and a second one, at a distance of ~ 12.1 m from the target, just before the switching magnet for proper charge state selection.

The DDCS for the collision energies 6, 9, 12, and 15 MeV and for the H_2 , He, Ne, and Ar gas targets, obtained in such double measurements for high and low $1s2s\ ^3S$ metastable fractions, are presented in Fig. 2. Single-collision conditions were tested and ensured for all targets. Accordingly, the Auger electron SDCS are obtained after integrating each Auger peak x over the electron energy ε' in the projectile frame DDCS spectrum, as

$$d\sigma_i[x] \equiv \frac{d\sigma_i[x]}{d\Omega'} = \int_{[x]} d\varepsilon' \frac{d^2\sigma_i[x]}{d\Omega' d\varepsilon'}, \quad (7)$$

for $i: 1, 2$ and $x: ^2S, ^2P_-, ^2P_+, ^4P$,

where the index $i = 1, 2$ refers to the two different measurements. Here $d\sigma_i[x]$ will be used as a shorthand for $\frac{d\sigma_i[x]}{d\Omega'}$ to avoid unnecessary clutter in the mathematical expressions to follow. Note that $d\sigma_i[x]$ are not *true* cross sections since they depend on the beam component content and therefore will be referred to as *apparent* cross sections.

From these double measurements, the ground- and metastable-state individual contributions to the production of the $1s2l2l'$ electronic configurations are extracted according to the following two requirements of the method:

- (a) The $1s2s2p\ ^4P$ state is produced solely from the $1s2s\ ^3S$ component by single-electron capture.
- (b) The $1s2p^2\ ^2D$ state is produced predominantly from the $1s^2\ ^1S$ ground-state component by the process of transfer excitation.

It should be noted here that the $1s2s2p\ ^4P$ is a long-lived state, which has certain implications for its detection efficiency that will be considered below. The true SDCS, $d\sigma_g[x]/d\Omega'$ and $d\sigma_m[x]/d\Omega'$, corresponding to the $1s^2\ ^1S$ ground and $1s2s\ ^3S$ metastable states, respectively, are then derived as [Ref. [41], Eqs. (A.12) and (A.13)]

$$\frac{d\sigma_m}{d\Omega'}[x] = \frac{d\sigma_2[x]d\sigma_1[{}^2D] - d\sigma_1[x]d\sigma_2[{}^2D]}{d\sigma_1[{}^2D] - d\sigma_2[{}^2D]}, \quad (8)$$

$$\frac{d\sigma_g}{d\Omega'}[x] = \frac{d\sigma_2[x]d\sigma_1[{}^4P] - d\sigma_1[x]d\sigma_2[{}^4P]}{d\sigma_1[{}^4P] - d\sigma_2[{}^4P]}, \quad (9)$$

for $d\sigma_1[x]$, $d\sigma_2[x]$, and x as in Eq. (7). In this paper, we focus on SEC to the *metastable* $1s2s\ ^3S$ component of the ion beam and therefore the determination of the SDCS, $d\sigma_m[x]/d\Omega'$. These SDCSs are reported for zero-degree measurements as $d\sigma[x](0^\circ)/d\Omega'$ (where we have dropped the implied m subscript) in Table V for the doublets 2S , $^2P_{\pm}$, and Table VI for the 4P , as well as in Fig. 5 for H_2 and He and Fig. 11 for Ne and Ar targets, respectively.

D. Determination of the metastable fraction

Our method, as can be seen from Eqs. (8) and (9), does not require the explicit determination of the beam metastable fractions $f_{3S}^{[1]}$ and $f_{3S}^{[2]}$. However, this information is implicit in Eqs. (8) and (9) and can be readily extracted as [see Ref. [41],

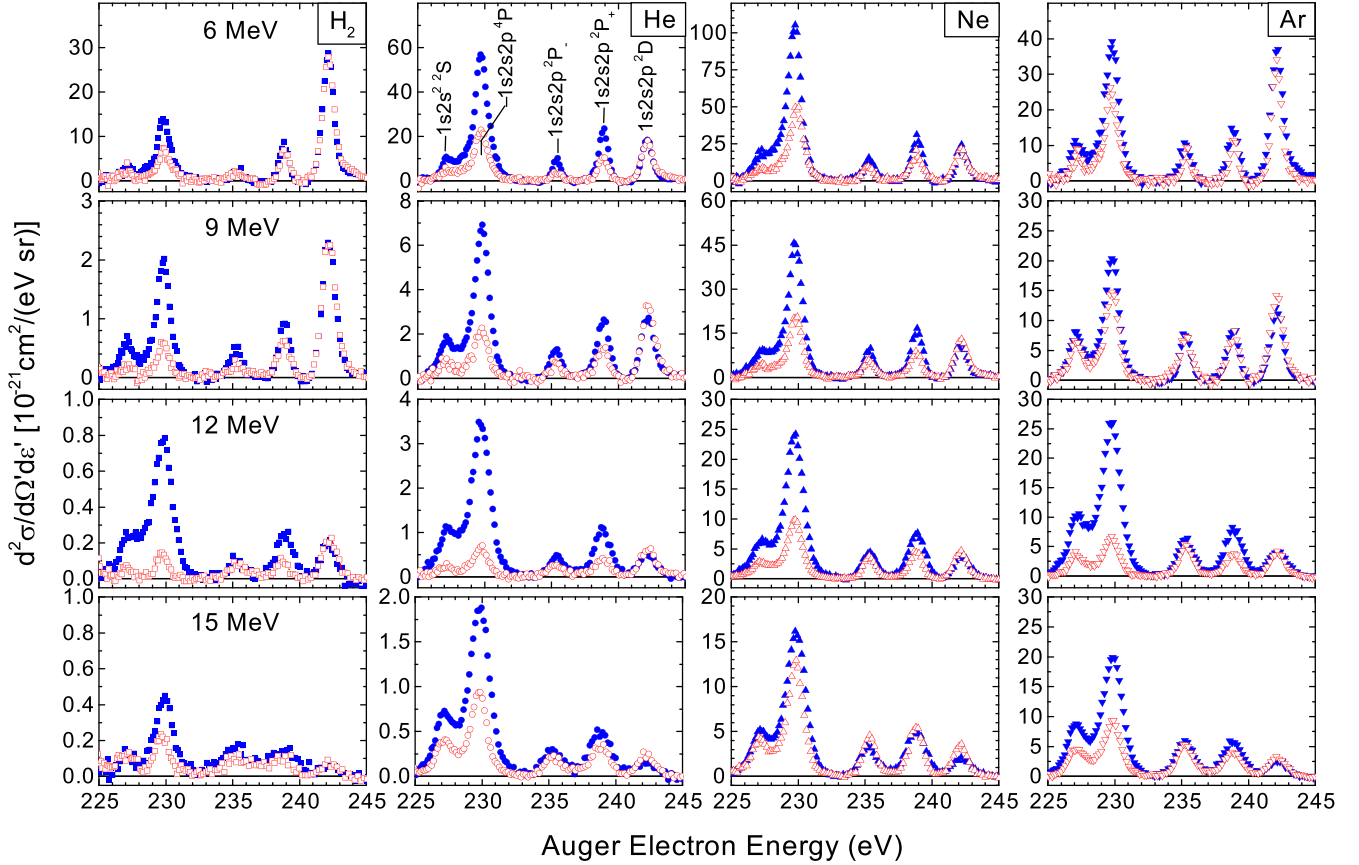


FIG. 2. Projectile rest frame 0° DDCS for collisions of 6, 9, 12, and 15 MeV (top to bottom) $C^{4+}(1s^2\ ^1S, 1s2s\ ^3S)$ mixed-state beams with H_2 , He, Ne, and Ar gas targets (left to right). The red symbols are electron spectra obtained from the low f_{3S} fraction beam content, using GTS or GPS. The blue symbols are spectra obtained from the high f_{3S} fraction beam content, using FTS or FPS, as evident from the enhanced yield of the $1s2s2p\ ^4P$ peak in the latter. See text for details on the ion-stripping procedures. The doubly excited states are identified by their Auger energies as shown for He at 6 MeV collision energy.

Eq. (A.14)]

$$f_{3S}^{[i]} = d\sigma_i[{}^4P] \frac{d\sigma_2[{}^2D] - d\sigma_1[{}^2D]}{d\sigma_2[{}^2D]d\sigma_1[{}^4P] - d\sigma_1[{}^2D]d\sigma_2[{}^4P]} \quad (10)$$

for $d\sigma_i[x]$ as in Eq. (7). The metastable fractions were determined from the apparent cross sections, obtained after integrating the Auger peaks in the DDCS spectra with the He target, and are shown in Fig. 3. The fractions obtained with H_2 targets were not used since they have much larger inherent uncertainties due to poorer statistics. High fractions were obtained using GPS (at $E_p = 6$ and 9 MeV) and FTS (at $E_p = 12$ and 15 MeV), while low fractions were obtained mostly using GTS. It is seen that over the projectile energy range used, both the high and the low values are fairly constant with average values of $(17.5 \pm 3.5)\%$ and $(5.5 \pm 1.5)\%$, respectively.

E. SDCS for collisions with heavy targets

In the case of heavy gas targets, like Ne and Ar used here, the requirement (b) above is not well fulfilled because the $1s2p^2\ ^2D$ state has a nonnegligible probability to be produced also from the $1s2s\ ^3S$ component [37], mostly due to the many more electrons available for SEC from the target L and M shells. Thus, in the case of Ne and Ar targets, Eqs. (8) and (9) are not valid anymore. In this case, however, it is

still possible to obtain SDCS with the additional information about the beam content, readily obtained from the previous

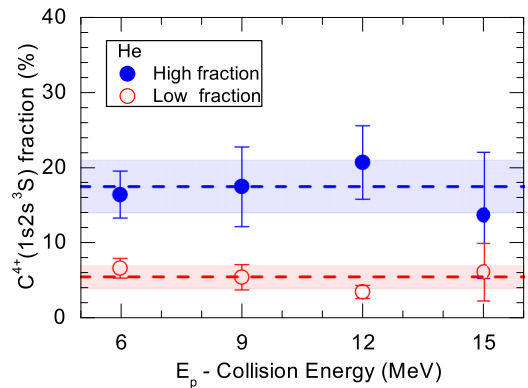


FIG. 3. Metastable state $C^{4+}(1s2s\ ^3S)$ fractions obtained with He targets. High fractions $f_{3S}^{[1]}$ (blue filled circles) were obtained with GPS (6 and 9 MeV) and FTS (12 and 15 MeV), while low fractions $f_{3S}^{[2]}$ (red open circles) were obtained with GTS, using Eq. (10). See text for details on the ion stripping processes. Dashed lines: Average values of $f_{3S}^{[1]} = (17.5 \pm 3.5)\%$ and $f_{3S}^{[2]} = (5.5 \pm 1.5)\%$. The shaded area around the dashed lines represents the uncertainty in these average fractions.

measurements with He or H₂ targets for which conditions (a) and (b) are valid, using Eq. (10). In our measurements, we performed the DDCS measurements for each stripping condition on all four targets, in sequence one after the other (proper flushing the gas delivery lines to clear any contaminants of the previous target is extremely important), thus ensuring the consistency of the beam metastable content used across all four gas targets.

For the heavier Ne and Ar targets, for each state x , the contributions from each beam component, $d\sigma_m[x]/d\Omega'$ and $d\sigma_g[x]/d\Omega'$, are then calculated from the following system of equations [see Eqs. (A.1) and (A.2) in Ref. [41]], which is always valid independent of any requirements such as (a) and (b) used above:

$$(1 - f_{3S}^{[1]}) \frac{d\sigma_g}{d\Omega'}[x] + f_{3S}^{[1]} \frac{d\sigma_m}{d\Omega'}[x] = d\sigma_1[x], \quad (11)$$

$$(1 - f_{3S}^{[2]}) \frac{d\sigma_g}{d\Omega'}[x] + f_{3S}^{[2]} \frac{d\sigma_m}{d\Omega'}[x] = d\sigma_2[x]. \quad (12)$$

The fractions $f_{3S}^{[1]}$ and $f_{3S}^{[2]}$, shown in Fig. 3, were computed from Eq. (10) using the apparent SDCS, $d\sigma_i[x]$ [Eq. (7)], determined from collisions with the He target under the requirements (a) and (b). Solving the system of two linear equations, Eqs. (11) and (12), for the two unknowns $d\sigma_g[x]/d\Omega'$ and $d\sigma_m[x]/d\Omega'$, where now the fractions $f_{3S}^{[1]}$ and $f_{3S}^{[2]}$ are known coefficients, we obtain

$$\frac{d\sigma_g}{d\Omega'}[x] = \frac{f_{3S}^{[2]} d\sigma_1[x] - f_{3S}^{[1]} d\sigma_2[x]}{f_{3S}^{[2]} - f_{3S}^{[1]}}, \quad (13)$$

$$\frac{d\sigma_m}{d\Omega'}[x] = \frac{(1 - f_{3S}^{[1]}) d\sigma_2[x] - (1 - f_{3S}^{[2]}) d\sigma_1[x]}{f_{3S}^{[2]} - f_{3S}^{[1]}}. \quad (14)$$

Equation (14) and the average metastable fractions determined from collisions with He (shown in Fig. 3, dashed lines) were used to compute the SDCS for the Ne and Ar targets (see Sec. IV).

F. The $1s2s2p$ 4P state solid angle correction

The 4P_J states are characterized by inherent total angular momentum J -dependent long lifetimes [49–51]. Thus, the three $1s2s2p$ 4P states, i.e., $^4P_{1/2}$, $^4P_{3/2}$, and $^4P_{5/2}$, Auger decay all along the projectile path from the gas cell to the spectrometer and even through it. This results in a variable detection solid angle $\Delta\Omega_J(V_p \tau_J, z)$, a function of the product of the J -level lifetime τ_J and the ion beam velocity V_p , as well as the acceptance solid angle $\Delta\Omega(z)$ at each point z of the decay. In a recent publication, we have treated this effect in a Monte Carlo-type simulation using the SIMION ion optics package to include any possible effects due to the injection lens [52], otherwise difficult to model analytically. There we introduced the effective solid angle correction factor G_{τ_J} as the ratio of the effective solid angle originating from a long-lived J level to the solid angle of a prompt state decaying inside the gas cell. The overall effective solid angle correction factor G_τ is then determined as the statistical averaging of the G_{τ_J} correction factors. Thus, we have

$$\overline{\Delta\Omega} = G_\tau \overline{\Delta\Omega_0}(s_0), \quad (15)$$

TABLE I. Solid angle correction factors G_τ and G_{τ_J} computed according to Eq. (16) and Eq. (17) used in the correction of the 4P_J ($J = 1/2, 3/2, 5/2$) solid angle $\Delta\Omega$ as given by (Eq. (15)).

E_p (MeV)	V_p (mm/ns)	G_τ	$G_{\tau_{1/2}}$	$G_{\tau_{3/2}}$	$G_{\tau_{5/2}}$
6.0	9.820	1.91	1.31	2.56	1.71
9.0	12.02	1.97	1.45	3.05	1.46
12	13.88	2.01	1.60	3.40	1.28
15	15.52	2.04	1.74	3.63	1.15

$$G_\tau = \frac{\sum_J (2J+1) \xi_J G_{\tau_J}}{\sum_J (2J+1) \xi_J}, \quad (16)$$

$$G_{\tau_J} = \frac{\overline{\Delta\Omega_J}}{\overline{\Delta\Omega_0}(s_0)}, \quad (17)$$

with the solid angles defined as [52]

$$\overline{\Delta\Omega_J} = \frac{1}{L_c} \int_{z'=0}^{L_c} dz' \int_{z=0}^{L_c/2+s_0-z'} dz \frac{\exp(-\frac{z}{V_p \tau_J})}{V_p \tau_J} \times \Delta\Omega_0(L_c/2 + s_0 - z' - z), \quad (18)$$

$$\overline{\Delta\Omega_0}(s_0) = \frac{1}{L_c} \int_{z'=0}^{L_c} dz' \Delta\Omega_0(L_c/2 + s_0 - z'), \quad (19)$$

$$\Delta\Omega_0(s) = 2\pi \left(1 - \frac{s}{\sqrt{r_0^2 + s^2}} \right), \quad (20)$$

with $\overline{\Delta\Omega_0}(s_0) = 1.515 \times 10^{-4}$ sr for the gas cell of effective length $L_c = 52.5$ mm centered at a distance $s_0 = 289$ mm from the lens entrance having an opening radius $r_0 = 2$ mm [52,53]. In the above calculations, we have used for the lifetimes $\tau_{1/2} = 2.94$ ns, $\tau_{3/2} = 7.10$ ns, and $\tau_{5/2} = 121.36$ ns [51] and for the Auger yields $\xi_{1/2} = 0.99$, $\xi_{3/2} = 0.94$, and $\xi_{5/2} = 1.00$ [54]. The correction factors G_τ and G_{τ_J} used for the 4P state are listed in Table I. All other states are prompt, and for these $G_\tau = 1$.

Our SIMION results were confirmed experimentally using Be-like mixed-state $C^{2+}(1s^2 2s^2 \ ^1S, 1s^2 2s 2p \ ^3P)$ beams [55]. There the $1s2s2p$ 4P state is produced from the $1s^2 2s 2p \ ^3P$ metastable state via $1s$ ionization, leading to the production of $1s2s2p$ 4P state free of cascade effects (described in more detail in Sec. IV), thus allowing for the accurate determination of the correction factor G_τ . Accordingly, the SDCS for the 4P state was also determined by Eq. (8), but corrected by further dividing by G_τ .

III. THEORY

The objectives of the present calculations are (i) to describe as precisely as possible the capture processes to produce C^{3+} in the autoionizing states observed experimentally, (ii) to predict the capture cross sections for higher levels of interest for cascade effects, (iii) to take into account the interelectronic repulsion and spin effects in up to three open shells, and (iv) to cover the entire energy range within the same treatment. Though requiring extremely intensive computations, we chose to solve nonperturbatively and within a full configuration

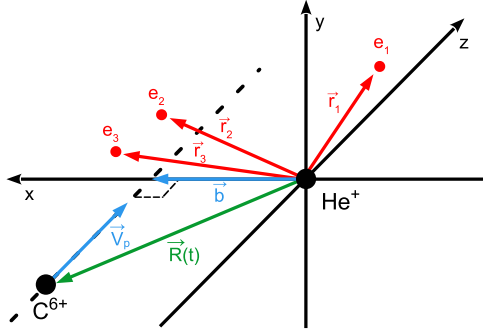


FIG. 4. Collision geometry. The impact parameter \mathbf{b} and velocity \mathbf{V}_p define the collision plane (xz) and $\mathbf{R}(t)$ the projectile (P) trajectory with respect to the target (T). The positions of the three electrons with respect to the target center are denoted $\mathbf{r}_1, \mathbf{r}_2, \mathbf{r}_3$. Note that for clarity we locate the origin of the reference on the target; this does not restrict the generality of our results, which are Galilean invariant.

interaction approach the eikonal equation [56], equivalent to the time-dependent Schrödinger equation (TDSE) in the semiclassical approximation (atomic units are used in the following),

$$i \frac{d}{dt} \psi(\mathbf{r}_1, \mathbf{r}_2, \mathbf{r}_3, t) = H \psi(\mathbf{r}_1, \mathbf{r}_2, \mathbf{r}_3, t). \quad (21)$$

The time t is related to the target (T)-projectile (P) relative position by the usual straight-line, constant velocity, relation, $\mathbf{R} = \mathbf{b} + \mathbf{V}_p t$, with \mathbf{b} and \mathbf{V}_p being the impact parameter and velocity, respectively, as seen in Fig. 4.

In Eq. (21) the Hamiltonian operator includes all Coulomb interactions between the nuclei and the three active electrons. Since two of the three active electrons correspond to the projectile, we performed calculations only for the He and dihydrogen targets, both modeled as an atom binding a unique, active electron. For the molecular target, we therefore do not take into account two-center effects (such as orientation, interferences, etc. [57–59]) due to the enormous increase that the two-center description would have required in computational effort. However, since the experiment was performed on an isotropic (nonoriented) target, our approach is a convenient and averaged alternative to model the electronic processes occurring during the collisions. The scattering wave function is expanded onto a set of asymptotic states (and pseudostates) ϕ_k^{PPP} and products $\phi_i^T \phi_j^{PP}$ of asymptotic states (and pseudostates) as

$$\psi(\mathbf{r}_1, \mathbf{r}_2, \mathbf{r}_3, t) = \sum_{i,j} c_{i,j}^{T,PP}(t) \phi_i^T \phi_j^{PP} + \sum_k c_k^{PPP}(t) \phi_k^{PPP}. \quad (22)$$

The superscripts T, PP, PPP denote states describing one, two, and three electrons on their respective centers (He, C^{4+} , and C^{3+} , respectively), including the usual energy phases, and for the projectile states, the electron translation factors $\exp(i\mathbf{V}_p \cdot \mathbf{r}_i - iV_p^2 t/2)$, to ensure Galilean invariance of the results [2]. Note that in Eq. (22), the electrons are treated as indistinguishable, and thus, the total wave function, as well as the atomic ϕ states, are fully antisymmetrized. The TDSE can then be written as a set of coupled differential equa-

tions for the expansion coefficients $c (\equiv c_{i,j}^{T,PP}$ or $c_k^{PPP})$, $\dot{\mathbf{c}}(t) = -i\mathbf{S}^{-1}\mathbf{M}\mathbf{c}(t)$, where \mathbf{S} is the overlap matrix and \mathbf{M} the coupling matrix, involving all couplings, notably the two-center interelectronic Coulomb repulsion. These equations are solved for an initial state i , [$C^{4+}(1s2s\ ^3S) + \text{He}(1s^2)$ in the present case] using the robust predictor-corrector time-step method and code developed by Shampine and Gordon [60]. The $c(t)$ coefficients are asymptotically probability amplitudes from which one gets the partial cross sections for production of the state $X (= {}^{2S+1}L)$ given by

$$\sigma[X](L, M_L) = 2\pi \int_0^{+\infty} b db |c_X(b, t \rightarrow \infty)|^2, \quad (23)$$

for all channels X spanned in our basis set. Here the state indicator $[X]$ may sometimes be omitted when clear, with the partial cross section then simply written as $\sigma(L, M_L)$, where M_L is the magnetic quantum number. In our approach, which does not include spin-orbit coupling, the total spin of the three-electron system is conserved and requires two independent calculations, one for the doublet and one for the quartet spin symmetries. The cross sections from these two series of calculations are therefore averaged by a factor 1/2 to ensure unitarity. Furthermore, the capture probabilities are rather small in the range of impact energies under consideration so that they are also multiplied by 2 to account for the two electrons of the target.

In more detail, the He, C^{4+} , and C^{3+} states are expressed as linear combinations of Gaussian-type orbitals (GTOs) and of spin-adapted products of these GTOs by diagonalisation of the respective atomic Hamiltonian operators within a full configuration interaction approach. The GTO exponents are optimized to minimize the number of GTOs, while ensuring accurate binding energies for the important states under consideration. The present calculations are based on a set of seven, seven, and 22 GTOs, that are centered on helium, hydrogen, and carbon, respectively. Their parameters are presented in Table II.

In our one-electron model of the helium target, the active electron of He is bound to He^+ by using a model potential, expressed as

$$V(r) = -\frac{1}{r} \sum_{i=1}^{13} c_i \exp(-\beta_i r^2), \quad (24)$$

with the values of the coefficients c_i and β_i given in Table III. These values were used to obtain a ground-state energy close to the first ionization energy and correct Coulombic limits at $r \rightarrow 0$ and $r \rightarrow +\infty$.

For the carbon center, the GTO set allows for obtaining accurate binding energies for the important states under consideration, i.e., $C^{4+}(1s2s\ ^3S)$ and $C^{3+}(1s2l' \ ^{2S+1}L)$, as presented in Table IV. Finally, the dynamical calculations for the doublet spin symmetry of the $C^{4+} + \text{He}$ ($C^{4+} + \text{H}$) collision system include 1794 (1807) bound, autoionizing

TABLE II. Orbital angular momentum quantum numbers l and exponents α of the GTOs $\mathcal{G}(r) = \mathcal{N}r^l \exp(-\alpha r^2)$ for hydrogen, helium, and carbon centers. The notation 4.931(-3) stands for 4.931×10^{-3} . Note that the number of GTOs for carbon is 22 considering the multiplicity of 3 for each of the $l = 1$ orbitals.

Hydrogen		Helium		Carbon	
l	α	l	α	l	α
0	4.931(-3)	0	7.250(-3)	0	5.500(-2)
0	2.457(-2)	0	2.903(-2)	0	1.298(-1)
0	1.591(-1)	0	1.163(-1)	0	3.064(-1)
0	4.360(-1)	0	4.656(-1)	0	7.231(-1)
0	1.152	0	1.864	0	1.707
0	1.905	0	7.466	0	4.028
0	6.850	0	2.990(1)	0	9.507
				0	2.244(1)
				0	5.296(1)
				0	1.250(2)
				1	2.600(-1)
				1	7.500(-1)
				1	2.449
				1	8.000

states and continuum pseudostates and, for the quartet spin symmetry, 802 (812), respectively. These numbers are limited by a maximal energy cutoff equal to about 31 a.u. relative to the ground states of the collision partners. The coupled differential equations were solved in a large time region corresponding to a projectile-target internuclear maximal distance equal to 100 a.u. The convergence of the results has been tested with respect to this parameter, as well as with respect to the size of the GTOs and state basis sets, and was found to be within 15% at worst for the channels under consideration.

The 3eAOCC calculations provide the probability amplitudes as a function of the impact parameter b from which the production cross sections can be readily evaluated using Eq. (23) for any of the $1s2l2l' {}^{2S+1}L$ channels treated. Following an Auger decay of the ${}^{2S+1}L$ state to a final ionic state with $L_f = 0$, as in the case of the $C^{4+}(1s^2)$ ground state examined here, the SDCS depend *only* on the cross sections of the magnetic states, $\sigma(L, M_L)$ of the autoionizing levels [64]. Thus, in this case, the Auger electron SDCSs can be computed at any observation angle θ (or θ' in the projectile rest frame) for the produced 2L doublet states using the well-known Auger electron angular distribution LS -coupling formula [64] written as an expansion of even-order Legendre polynomials, $P_k(\cos \theta')$:

$$\frac{d\sigma[{}^2L]}{d\Omega'}(\theta) = \bar{\xi}[{}^2L] \frac{\sigma_{\text{tot}}[{}^2L]}{4\pi} \sum_{k=0, \text{even}}^{2L} A_k(L) P_k(\cos \theta'), \quad (25)$$

where the total LS -multiplet production doublet cross section $\sigma_{\text{tot}}[{}^2L]$ is computed as

$$\sigma_{\text{tot}}[{}^2L] = \sum_{M_L=-L}^L \sigma(L, |M_L|). \quad (26)$$

The projectile rest frame emission angle θ' in Eq. (25) is related to the electron laboratory frame emission angle θ with respect to the direction of the projectile velocity by the frame

transformation relation:

$$\cos \theta' = \frac{-\zeta' \tan^2 \theta \pm \sqrt{1 + (1 - \zeta'^2) \tan^2 \theta}}{1 + \tan^2 \theta}, \quad (27)$$

with

$$\zeta' = \frac{V_p}{v'_A} = \sqrt{\frac{t_p}{\epsilon'_A}}, \quad (28)$$

where the Auger electron energy $\epsilon'_A = 1/2 m v'_A{}^2$ and the cusp energy t_p as already defined in Eq. (6). The \pm sign in Eq. (27) refers to the forward (+) or backward (-) emitted Auger electron [32].

In Eq. (25), $\bar{\xi}[{}^2L]$ is the mean Auger yield of the LS multiplet (usually computed as the statistical average over its J components ξ_J) given in general by

$$\bar{\xi}[{}^{2S+1}L] \equiv \frac{\sum_{J=L-S}^{J=L+S} (2J+1) \xi_J}{(2S+1)(2L+1)}. \quad (29)$$

Finally, the angular distribution parameters A_k [64] are in general complicated functions of partial cross sections $\sigma(SLJ)$, the interfering phases of the emitted l, j partial Auger waves and the reduced Auger matrix elements of the $SLJ \rightarrow S_f L_f J_f$ Auger transition. However, in the case where just a *single* l, j Auger partial wave is emitted, these coefficients are much simplified and independent of the phases and the reduced Auger matrix elements. This is always the case when the final ionic states $S_f L_f J_f$ have $J_f = 0$ [64,65], as in the case here, where the final ionic state is the $C^{4+}(1s^2 {}^1S)$ ground state with $S_f = L_f = J_f = 0$. For an isolated SLJ resonance these have been computed within the LSJ intermediate coupling [65,66]. If the SLJ resonances are completely unresolved, their contributions have to be added coherently within the same LS multiplet (case of *totally* overlapping resonances). The expression for A_k then for $L_f = 0$ and $S_f = S \pm 1/2$ can be shown to be given by [see Table I in Mehlhorn and Taulbjerg [64] or Kabachnik *et al.* [67] Eqs. (12) and (13)]

$$A_k(L) = \alpha_k(L) \mathcal{A}_{k0}(L), \quad (30)$$

with the anisotropy coefficient $\alpha_k[L]$ given by [67]

$$\alpha_k(L) = (-1)^L \sqrt{(2L+1)(2k+1)} \begin{pmatrix} L & L & k \\ 0 & 0 & 0 \end{pmatrix}, \quad (31)$$

and the alignment parameter $\mathcal{A}_{k0}[L]$ given by [see Ref. [67], p. 4655]

$$\begin{aligned} \mathcal{A}_{k0}(L) &= \frac{\sqrt{(2L+1)(2k+1)}}{\sum_{M_L} \sigma(L, |M_L|)} \\ &\times \sum_{M_L=-L}^L (-1)^{L-M_L} \begin{pmatrix} L & L & k \\ M_L & -M_L & 0 \end{pmatrix} \sigma(L, |M_L|). \end{aligned} \quad (32)$$

For the $S = 1/2, L = 1$ case of interest here (i.e., the ${}^2P_{\pm}$ states), we have only an A_2 term. Evaluating according to

TABLE III. Coefficients and exponents used to represent the system $\text{He}^+ + e^-$ by the model potential defined in Eq. (24).

i	1	2	3	4	5	6	7	8	9	10	11	12	13
c_i	1.0	0.02122	0.23856	0.24184	0.18409	0.12201	0.13192	0.01928	0.10648	0.10665	-0.04115	-0.07789	-0.07425
β_i	0.0	0.73506	4.59598	13.37885	47.82184	260.82361	1.78475	0.50641	1.07305	2.38839	12.09488	30.87964	153.60719

Eqs. (31) and (32) and (26), we have (see Ref. [64], Table 1)

$$\begin{aligned}
\alpha_2(L=1) &= -\sqrt{2}, \\
\mathcal{A}_{20}(L=1) &= \sqrt{2} \frac{[\sigma(1,1) - \sigma(1,0)]}{\sigma(1,0) + 2\sigma(1,1)}, \\
\mathcal{A}_2(L=1) &= \alpha_2(L=1)\mathcal{A}_{20}(L=1) \\
&= 2 \frac{\sigma(1,0) - \sigma(1,1)}{\sigma(1,0) + 2\sigma(1,1)}. \quad (33)
\end{aligned}$$

For $L=0$, only $k=0$ survives in the summation of Eq. (25) giving $A_0=1$, consistent with the expected isotropic emission.

For $\theta=0^\circ$, as in our ZAPS measurements, we have from Eq. (27) $\cos\theta'=\pm 1$ with $P_k(\pm 1)=1$ (for k even). Then, directly from Eqs. (25) and (33) for $L=0,1$, we have for the levels 2S and ${}^2P_{\pm}$, respectively:

$$\begin{aligned}
\frac{d\sigma[{}^2S]}{d\Omega'}(\theta=0^\circ) &= \bar{\xi}[{}^2S] \frac{\sigma[{}^2S](0,0)}{4\pi}, \quad (34) \\
\frac{d\sigma[{}^2P_{\pm}]}{d\Omega'}(\theta=0^\circ) &= 3\bar{\xi}[{}^2P_{\pm}] \frac{\sigma[{}^2P_{\pm}](1,0)}{4\pi}, \quad (35)
\end{aligned}$$

and thus the $\theta=0^\circ$ SDCS are seen to be sensitive only to the $M_L=0$ component of the partial cross sections. For measurements at $\theta \neq 0^\circ$, no such simplification takes place and all M_L values come into play [68,69]. Since for low- Z_p ions the spin-orbit interaction is negligible, the spin has a negligible effect on the production of the resonances. Thus, Eq. (35) was assumed to be a good approximation for the $1s2s2p\ {}^4P$ state too. The C^{3+} KLL Auger yields ξ_j are all very close to 1, and we have therefore taken $\bar{\xi}[{}^{2S+1}L]=1$ for all $L=0,1$.

TABLE IV. Binding energies (in a.u.) of some of the important C^{4+} and C^{3+} states included in our basis set used in the close-coupling calculations. The values are relative to the corresponding ground states. For comparison, the last line shows the values from other sources, as indicated.

C^{4+}		C^{3+}			
$1s2s$		$1s2s2p$		$1s2s3s$	$1s2s3p$
3S	4P	${}^2P_-$	${}^2P_+$	4S	4P
10.90	10.73	10.95	11.11	12.17	12.55
10.99 ^a	10.77 ^b	10.99 ^b	11.15 ^b	12.22 ^c	12.31 ^b

^aEngstrom *et al.* [61] and NIST Atomic Spectra Database [62].

^bChen [54].

^cDumont *et al.* [63].

IV. RESULTS AND DISCUSSION

In this section we present our results related to the SEC process in fast collisions of pre-excited $\text{C}^{4+}(1s2s\ {}^3S)$ beams with gas targets [see Eq. (1)].

A. H_2 and He targets

In Fig. 5 and Tables V and VI, we present the experimental and theoretical SDCSs for the $1s2s^2\ {}^2S$, $1s2s2p\ {}^2P_-$, $1s2s2p\ {}^2P_+$, and $1s2s2p\ {}^4P$ states obtained in collisions of the pre-excited $\text{C}^{4+}(1s2s\ {}^3S)$ beams with H_2 and He targets. The experimental SDCSs were obtained after a straightforward integration of the peaks in the DDSCS spectra according to Eq. (7). Special care was taken for the proper background fit and subtraction, since our two-spectra measurement technique is sensitive in electron yield differences. Only the 2S peak, residing on the low energy wing of the $1s2s2p\ {}^4P$ peak, was fitted to extract the SDCS. Moreover, in the case of the $1s2s2p\ {}^4P$ peak, the SDCS, obtained after subtracting the fitted 2S peak, was corrected by further dividing it by the solid angle correction factor G_τ , listed in Table I according to projectile energy E_p .

In Fig. 5 reasonable agreement between the calculations and the measurements can be observed. For the case of He, the SDCS calculations are seen to be larger than the measurements (close to an average factor of 2) except at the higher projectile energy of 15 MeV, for which the agreement is very good. The strongest deviations are for the 2S state, possibly due to the difficulty to extract the Auger yield from the low-energy tail of the 4P peak (see Fig. 2). Indeed, for the lowest energies, the 2S presents a much lower yield compared to the 4P , inherently increasing its uncertainty. However, at the highest energy (15 MeV), the 2S yield is relatively increased, improving its accuracy, as evident from the improved agreement with the theoretical results. Even better agreement is seen for the case of H_2 , although the statistical error bars are larger than for He. This latter point is attributed to the fact that H_2 has smaller SEC cross sections compared to He, even by an order of magnitude and, thus, suffers from poorer statistics in the measurements. Indeed, for the 2S state at the highest projectile energy (15 MeV), corresponding to the smallest cross section of the set of measurements for H_2 targets, the SDCS could not be obtained within a reasonable error bar.

B. Cascade feeding of the $1s2s2p\ {}^4P$

For the $1s2s2p\ {}^4P$ state, which corresponds to the strongest capture channel under consideration, contributions from selective cascade feeding [18] were also included in the 3eAOCC results, as discussed in detail in Ref. [70]. SEC may result in both doublet and quartet $1s2snl\ {}^{2,4}L$, ($n \geq 2$) states. Configurations with $n > 2$ may decay to the $1s2s2p$

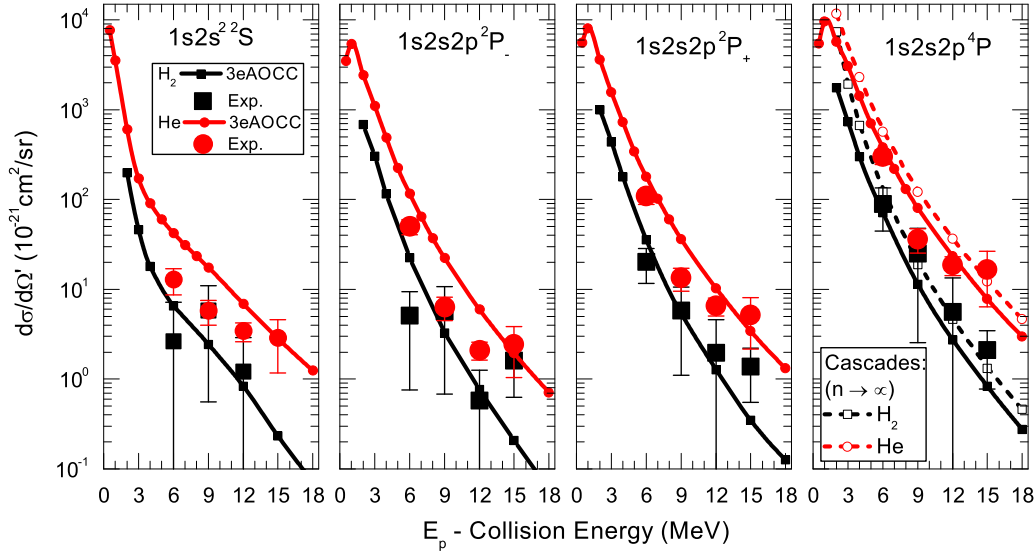


FIG. 5. 0° Auger electron SDCS for the $1s2s^2\ ^2S$, $1s2s2p\ ^2P_-$, $1s2s2p\ ^2P_+$, and $1s2s2p\ ^4P$ states obtained in collisions of $C^{4+}(1s2s\ ^3S)$ with H_2 and He targets. Symbols: Measurements (squares, H_2 ; circles, He targets). Only statistical uncertainties are shown. Solid lines with symbols: 3eAOCC calculations (black, H_2 ; red, He). Dotted lines also include the cascade feeding of the $1s2s2p\ ^4P$ states from higher lying ($1s2snl\ ^4L$, $n > 2$) quartet states and listed under the (SEC+C) columns in Table VI, computed according to Eq. (36). The lines correspond to interpolations between the theoretical points to guide the eye.

configuration radiatively, by E1 transitions, thus increasing its initial population. However, the $1s2snl\ ^2L$ doublets have strong Auger decay rates to the $1s^2$ ground state and are quickly depleted. Thus, they do not significantly affect the initial population of the $1s2s2p\ ^2P$ states. On the contrary, the $1s2snl\ ^4L$ quartet states have very weak Auger decay rates to the $1s^2$ ground state and thus radiatively decay via cascades to the lowest quartet state, i.e., the $1s2s2p\ ^4P$, acts as a kind of “excited ground state” for the radiative cascading of these higher lying $nl\ ^4L$ quartet states [5,18,70]. Recently, we have presented a detailed treatment of the selective cascade feeding mechanism in carbon resulting in the significant increase of the population of the $1s2s2p\ ^4P$ state [70]. Our results include cross sections for cascade feeding from the $n = 3$, $n = 3 + n = 4$ shells and an extrapolation to include all $n \rightarrow \infty$ according to the well known n^{-3} law for the SEC process [5,71] as listed in Table VII. Here we note that the $l = 2$ and $l = 3$ (e.g., $3d, 4d, 4f$) orbitals were not included in our three-active electron calculations (3eAOCC), and the related cross sections were therefore evaluated within a *one*-electron treatment (1eAOCC).

Accordingly, for the total contribution to the 4P including cascade repopulation (SEC+C), the $\theta = 0^\circ$ SDCS is given by

$$\frac{d\sigma[^4P]}{d\Omega'}(0^\circ) = 3\bar{\xi}[^4P] \frac{(\sigma[^4P](1, 0) + \sigma_0^C[n \rightarrow \infty])}{4\pi} \quad (36)$$

with $\bar{\xi}[^4P] = 1$, as previously. Here $\sigma_0^C[n \rightarrow \infty]$ is the cascade contribution to the $M_L = 0$ magnetic state of the 4P given in Table VII and computed in our cascade analysis presentation [70]. The above SDCS for the 4P with and without cascade feeding are shown in Fig. 5. As can be seen, cascade feeding seems to account for an overall increase of $\sim 70\%$ for H_2 and $\sim 55\%$ for He of the SDCS for the experimental

collision energies. For He, the SDCS calculations are seen to be larger than the measurements, while for H_2 the agreement is slightly better, further improving when cascade feeding is included. The calculated total cross sections for nl SEC to the $1s2snl\ ^4L$ levels leading to cascade feeding of the 4P are also shown as a function of collision energy in Fig. 6.

C. Impact parameter dependence

In Fig. 7 the impact parameter b dependence of the reduced probability $bP(b)$ for the production of the $1s2s^2\ ^2S$, $1s2s2p\ ^2P_-$, $1s2s2p\ ^2P_+$, and $1s2s2p\ ^4P$ states is presented for the He target. For all three P states a similar behavior is observed. The production probability follows a typical bell-shape behavior with an increase up to b ranging between 0.5 and 1.0 a.u., followed by an exponential decay. The maximum is seen to shift to smaller impact parameters with increasing projectile energy. For example, in the case of the $1s2s2p\ ^4P$ state, the maximum is located around $b = 1$ a.u. for the smallest energy $E_p = 2$ MeV, while around $b = 0.5$ a.u. for the highest energy, $E_p = 18$ MeV. This indicates that in the range of energy under consideration the main contribution to the cross sections comes from head-on collisions, as expected.

For the $1s2s^2\ ^2S$ state, the behavior of the reduced probabilities with respect to the impact parameter have a special feature, not observed in the P states: they show two maxima, separated by a minimum. These minima are similar to the Cooper minima observed in atomic photoionization spectra for states which possess nodes [72]. Indeed, we observe such structures for electron transfer to $2s$, but not to $2p$ orbitals, so they can be called “Cooper-like minima,” as also advocated in photoionization of diatomic molecules [73]. It is then quite interesting to observe that at low energies, the important contribution to the cross sections is located at large impact

TABLE V. Experimental and theoretical 0° Auger electron SDCS for the doublets $1s2s^2\ ^2S$, $1s2s2p\ ^2P_-$, and $1s2s2p\ ^2P_+$ obtained in $C^{4+}(1s2s\ ^3S) + H_2$, He, Ne, and Ar collisions. The theoretical SDCS were obtained applying Eqs. (34) and (35). The 3eAOCC partial cross sections, $\sigma(L, M_L)$, obtained using Eq. (23) are also listed. Measurements show only statistical errors. The SDCS, $(\frac{d\sigma(0^\circ)}{d\Omega'})$ are also shown in Fig. 5, while $\sigma(L, M_L)$ are also shown in Fig. 8. Entries indicated by – means no result was acquired, while an empty (blank) entry means this entry does not apply. Numerical format as in Table II.

E_p (MeV)	H ₂		H(1s)		He		He(1s)		Ne		Ar	
	Expt.	$\frac{d\sigma(0^\circ)}{d\Omega'}$ ($\times 10^{-21}$ cm ² /sr)	$\frac{d\sigma(0^\circ)}{d\Omega'}$ ($\times 10^{-21}$ cm ² /sr)	$\sigma(L, 0)$ $\sigma(1, 1)$ ($\times 10^{-21}$ cm ²)	Expt.	$\frac{d\sigma(0^\circ)}{d\Omega'}$ ($\times 10^{-21}$ cm ² /sr)	$\frac{d\sigma(0^\circ)}{d\Omega'}$ ($\times 10^{-21}$ cm ² /sr)	$\sigma(L, 0)$ $\sigma(1, 1)$ ($\times 10^{-21}$ cm ²)	Expt.	$\frac{d\sigma(0^\circ)}{d\Omega'}$ ($\times 10^{-21}$ cm ² /sr)	Expt.	$\frac{d\sigma(0^\circ)}{d\Omega'}$ ($\times 10^{-21}$ cm ² /sr)
<u>$L = 0:1s2s^2\ ^2S$</u>												
0.5	–	–	–	–	–	7.64(3)	9.60(4)	–	–	–	–	–
1	–	–	–	–	–	3.51(3)	4.41(4)	–	–	–	–	–
2	–	1.98(2)	2.49(3)	–	–	6.02(2)	7.56(3)	–	–	–	–	–
3	–	4.61(1)	5.79(2)	–	–	1.70(2)	2.14(3)	–	–	–	–	–
4	–	1.81(1)	2.27(2)	–	–	9.07(1)	1.14(3)	–	–	–	–	–
5	–	–	–	–	–	5.99(1)	7.53(2)	–	–	–	–	–
6	2.6 ± 4.5	6.51	8.18(1)	–	13 ± 4.1	4.22(1)	5.31(2)	–	40 ± 12	–	28 ± 8.3	–
7	–	–	–	–	–	3.10(1)	3.89(2)	–	–	–	–	–
8	–	–	–	–	–	2.32(1)	2.92(2)	–	–	–	–	–
9	5.8 ± 5.2	2.44	3.07(1)	–	5.8 ± 1.8	1.74(1)	2.18(2)	–	28 ± 8.4	–	13 ± 4.4	–
12	1.2 ± 1.7	8.36(–1)	1.05(1)	–	3.4 ± 0.83	6.86	8.62(1)	–	14 ± 4.1	–	51 ± 16	–
15	–	2.33(–1)	2.93	–	2.9 ± 1.7	2.85	3.58(1)	–	4.9 ± 1.2	–	30 ± 8.7	–
18	–	7.20(–2)	9.05(–1)	–	–	1.24	1.56(1)	–	–	–	–	–
<u>$L = 1:1s2s2p\ ^2P_-$</u>												
0.5	–	–	–	–	–	3.50(3)	1.47(4)	2.22(4)	–	–	–	–
1	–	–	–	–	–	5.38(3)	2.25(4)	1.19(4)	–	–	–	–
2	–	6.89(2)	2.89(3)	9.63(2)	–	2.42(3)	1.01(4)	3.18(3)	–	–	–	–
3	–	3.05(2)	1.28(3)	2.94(2)	–	1.10(3)	4.59(3)	1.07(3)	–	–	–	–
4	–	1.16(2)	4.86(2)	1.11(2)	–	4.88(2)	2.05(3)	4.44(2)	–	–	–	–
5	–	–	–	–	–	2.24(2)	9.38(2)	2.08(2)	–	–	–	–
6	5.1 ± 4.3	2.25(1)	9.44(1)	2.08(1)	50. ± 9.8	1.15(2)	4.83(2)	1.04(2)	46 ± 12	–	39 ± 10.	–
7	–	–	–	–	–	6.41(1)	2.67(2)	5.41(1)	–	–	–	–
8	–	–	–	–	–	3.71(1)	1.56(2)	2.96(1)	–	–	–	–
9	5.7 ± 5.0	3.28	1.38(1)	3.08	6.3 ± 1.9	2.22(1)	9.28(1)	1.76(1)	34 ± 8.7	–	7.4 ± 3.6	–
12	0.58 ± 0.68	7.67(–1)	3.21	9.19(–1)	2.1 ± 0.47	5.97	2.50(1)	5.18	21 ± 5.3	–	32 ± 8.8	–
15	1.6 ± 0.98	2.11(–1)	8.85(–1)	3.02(–1)	2.4 ± 1.4	1.94	8.13	1.86	9.0 ± 1.9	–	23 ± 6.0	–
18	–	5.99(–2)	2.51(–1)	9.90(–2)	–	7.19(–1)	3.01	8.27(–1)	–	–	–	–
<u>$L = 1 : 1s2s2p\ ^2P_+$</u>												
0.5	–	–	–	–	–	5.55(3)	2.32(4)	2.31(4)	–	–	–	–
1	–	–	–	–	–	8.04(3)	3.37(4)	1.37(4)	–	–	–	–
2	–	1.00(3)	4.21(3)	1.56(3)	–	3.60(3)	1.51(4)	4.73(3)	–	–	–	–
3	–	4.40(2)	1.84(3)	5.44(2)	–	1.56(3)	6.55(3)	1.90(3)	–	–	–	–
4	–	1.79(2)	7.50(2)	2.13(2)	–	7.26(2)	3.04(3)	8.67(2)	–	–	–	–
5	–	–	–	–	–	3.40(2)	1.43(3)	4.30(2)	–	–	–	–
6	20. ± 8.5	3.55(1)	1.49(2)	4.19(1)	109 ± 20.	1.80(2)	7.53(2)	2.24(2)	98 ± 25	–	54 ± 15	–
7	–	–	–	–	–	1.02(2)	4.28(2)	1.21(2)	–	–	–	–
8	–	–	–	–	–	5.98(1)	2.50(2)	7.00(1)	–	–	–	–
9	5.8 ± 4.7	5.34	2.24(1)	6.74	13 ± 3.8	3.61(1)	1.51(2)	4.42(1)	76 ± 21	–	13 ± 3.9	–
12	2.0 ± 2.6	1.28	5.35	2.20	6.5 ± 1.5	1.02(1)	4.27(1)	1.49(1)	54 ± 15	–	66 ± 20.	–
15	1.4 ± 0.83	3.48(–1)	1.46	8.96(–1)	5.1 ± 3.0	3.44	1.44(1)	5.83	22 ± 5.6	–	36 ± 10.	–
18	–	1.28(–1)	5.37(–1)	2.79(–1)	–	1.32	5.54	2.54	–	–	–	–

parameters and related to trajectories for which the main part of the electronic cloud of the carbon $2p$ orbital, i.e., beyond the node, overlaps optimally with the target $1s$ orbital at the turning point. On the other hand, for the production of the $1s2s2p\ ^2P$ states, this steric effect is absent, explaining the rather smooth behavior of the probabilities in this case. For

increasing energies, the collisions to produce any of these states become more and more head-on, explaining the more rapid decay of the cross sections for the 2S state. Note that the second probability maximum can still be observed, but is an order of magnitude less important than the first and therefore does not contribute to the cross sections.

TABLE VI. Same as for Table V, but for $1s2s2p^4P$ states including cascade repopulation (SEC+C) [70]. The theoretical SDCS at $\theta = 0^\circ$ were obtained applying Eq. (36).

E_p (MeV)	H ₂		Theory H (1s)			He		Theory He (1s)			Ne	Ar
	Expt.	(SEC+C)	(SEC)		Expt.	(SEC+C)	(SEC)		Expt.	Expt.		
	$\frac{d\sigma(0^\circ)}{d\Omega'}$ ($\times 10^{-21}$ cm ² /sr)	$\frac{d\sigma(0^\circ)}{d\Omega'}$ ($\times 10^{-21}$ cm ² /sr)	$\frac{d\sigma(0^\circ)}{d\Omega'}$	$\sigma(1, 0)$ ($\times 10^{-21}$ cm ²)	$\sigma(1, 1)$ ($\times 10^{-21}$ cm ²)	$\frac{d\sigma(0^\circ)}{d\Omega'}$ ($\times 10^{-21}$ cm ² /sr)	$\frac{d\sigma(0^\circ)}{d\Omega'}$ ($\times 10^{-21}$ cm ² /sr)	$\frac{d\sigma(0^\circ)}{d\Omega'}$	$\sigma(1, 0)$ ($\times 10^{-21}$ cm ²)	$\sigma(1, 1)$ ($\times 10^{-21}$ cm ²)	$\frac{d\sigma(0^\circ)}{d\Omega'}$ ($\times 10^{-21}$ cm ² /sr)	$\frac{d\sigma(0^\circ)}{d\Omega'}$ ($\times 10^{-21}$ cm ² /sr)
0.5	—	—	—	—	—	—	—	5.43(3)	2.27(4)	5.47(4)	—	—
1	—	—	—	—	—	—	—	9.58(3)	4.01(4)	3.13(4)	—	—
2	—	7.38(3)	1.75(3)	7.33(4)	2.39(4)	—	1.17(4)	5.70(3)	2.39(4)	8.88(3)	—	—
3	—	1.94(3)	7.33(2)	3.07(3)	7.80(2)	—	—	3.05(3)	1.28(4)	3.15(3)	—	—
4	—	6.69(2)	3.01(2)	1.26(3)	3.05(2)	—	2.31(3)	1.43(3)	5.98(3)	1.34(3)	—	—
5	—	—	—	—	—	—	—	6.99(2)	2.93(3)	6.42(2)	—	—
6	89±45	1.23(2)	7.13(1)	2.99(2)	6.07(1)	302 ± 57	5.70(2)	3.80(2)	1.59(3)	3.33(2)	430 ± 121	130 ± 36.1
7	—	—	—	—	—	—	—	2.19(2)	9.19(2)	1.80(2)	—	—
8	—	—	—	—	—	—	—	1.31(2)	5.48(2)	1.03(2)	—	—
9	25 ± 23	1.89(1)	1.13(1)	4.75(1)	9.76	36 ± 11	1.21(2)	8.00(1)	3.35(2)	6.39(1)	204 ± 57.9	55.9 ± 14.7
12	5.6 ± 7.8	4.66	2.73	1.14(1)	3.18	19 ± 4.4	3.63(1)	2.32(1)	9.73(1)	2.12(1)	142 ± 41.3	188 ± 57.5
15	2.1 ± 1.3	1.42	8.32(-1)	3.49	1.25	17 ± 10.	1.22(1)	7.84	3.28(1)	8.28	58.4 ± 15.9	119 ± 34.7
18	—	4.63(-1)	2.75(-1)	1.15	4.80(-1)	—	4.63(-1)	2.96	1.24(1)	3.76	—	—

D. Partial cross section contributions

In Fig. 8 and Tables V and VI, 3eAOCC partial cross sections $\sigma(L = 1, |M_L| = 0, 1)$ for the production of the $1s2s^2\ ^2S$, $1s2s2p\ ^2P_-$, $1s2s2p\ ^2P_+$, and $1s2s2p\ ^4P$ states for He targets are presented. It is evident that the major contribution to the P states comes from the $M_L = 0$ magnetic states.

This implies an important alignment of the P states produced by SEC. This alignment favors ZAPS measurements, since at $\theta = 0^\circ$ observation, only the $M_L = 0$ magnetic states can be observed (for $L_f = 0$ final ionic states as here), as also mentioned earlier. Similar results are also found for H (not shown).

TABLE VII. Calculated $1s2snl\ ^4L$ cross sections ($\sigma[nl\ ^4L]$) due to nl SEC and selective cascade feeding of the $1s2s2p\ ^4P$ from $n = 3$ and $n = 4$ levels in collisions of $C^{4+}(1s2s\ ^3S)$ with He (1s) and H (1s). $\sigma_0^C[n = 3]$, $\sigma_0^C[n = 3 + n = 4]$ and $\sigma_0^C[n \rightarrow \infty]$ are the cross sections for the cascade contributions to the $M_L = 0$ magnetic states of $1s2s2p\ ^4P$ from $n = 3$, $n = 3 + n = 4$ and extrapolated to include all higher lying $n \rightarrow \infty$ (i.e., $3 \leq n \leq \infty$), respectively [70]. Finally, R is the ratio of 4P to $^2P_\pm$ cross sections as given by Eq. (38) and already presented in Refs. [28,70]. Numerical format as in Table II.

E_p (MeV)	$\sigma[2p\ ^4P]$	$\sigma[3s\ ^4S]$	$\sigma[3p\ ^4P]$	$\sigma[3d\ ^4D]^a$	$\sigma[4s\ ^4S]$	$\sigma[4p\ ^4P]$	$\sigma[4d\ ^4D]^a$	$\sigma[4f\ ^4F]^a$	$\sigma_0^C[n=3]$	$\sigma_0^C[n = 3 + n = 4]$	$\sigma_0^C[n \rightarrow \infty]$	R
				($\times 10^{-21}$ cm ²)						($\times 10^{-21}$ cm ²)		
He (1s)												
2.0	4.16(4)	1.91(3)	1.57(4)	1.88(4)	9.38(2)	8.37(3)	1.09(4)	6.78(2)	1.01(4)	1.67(4)	2.52(4)	1.95
4.0	8.66(3)	4.54(2)	3.90(3)	2.01(3)	1.82(2)	2.10(3)	5.93(2)	2.71	1.61(3)	2.53(3)	3.71(3)	1.91
6.0	2.26(3)	1.66(2)	9.63(2)	2.53(2)	7.83(1)	4.64(2)	9.07(1)	6.99(-1)	3.35(2)	5.36(2)	7.95(2)	1.93
9.0	4.63(2)	6.32(1)	2.24(2)	2.77(1)	2.20(1)	1.02(2)	9.51	6.09(-2)	7.57(1)	1.18(2)	1.72(2)	2.08
12.0	1.40(2)	2.40(1)	6.68(1)	5.66	1.12(1)	3.03(1)	2.69	1.79(-2)	2.34(1)	3.72(1)	5.49(1)	2.25
15.0	4.94(1)	8.97	2.24(1)	1.47	4.06	9.83	6.72(-1)	4.21(-3)	8.02	1.25(1)	1.84(1)	2.27
18.0	1.99(1)	3.80	8.35	4.71(-1)	1.70	3.62	2.14(-1)	1.00(-3)	3.12	4.83	7.03	2.27
H (1s)												
2.0	1.21(4)	9.35(2)	6.38(3)	1.65(4)	8.99(2)	4.44(3)	1.47(4)	1.37(3)	7.90(3)	1.48(4)	2.36(4)	4.36
3.0	4.63(3)	1.55(2)	2.37(3)	2.91(3)	1.55(2)	1.78(3)	2.58(3)	7.67(1)	1.80(3)	3.23(3)	5.06(3)	2.61
4.0	1.87(3)	7.83(1)	9.59(2)	7.75(2)	3.63(1)	6.69(2)	6.36(2)	9.42	5.98(2)	1.01(3)	1.54(3)	2.27
6.0	4.20(2)	3.61(1)	2.12(2)	7.33(1)	1.62(1)	1.20(2)	2.82(1)	5.87(-1)	1.06(2)	1.54(2)	2.17(2)	2.12
9.0	6.70(1)	9.99	3.24(1)	4.47	5.02	1.60(1)	3.10	2.75(-2)	1.54(1)	2.26(1)	3.18(1)	2.20
12.0	1.78(1)	2.59	9.17	8.75(-1)	1.04	4.57	2.74(-1)	2.18(-3)	4.16	5.87	8.07	2.27
15.0	5.99	7.82(-1)	2.89	2.07(-1)	3.90(-1)	1.33	7.17(-2)	6.04(-4)	1.28	1.80	2.47	2.37
18.0	2.11	2.40(-1)	9.62(-1)	5.85(-2)	1.17(-1)	4.30(-1)	1.60(-2)	9.29(-5)	4.15(-1)	5.79(-1)	7.89(-1)	2.46

^a1eAOCC nl SEC results (see text).

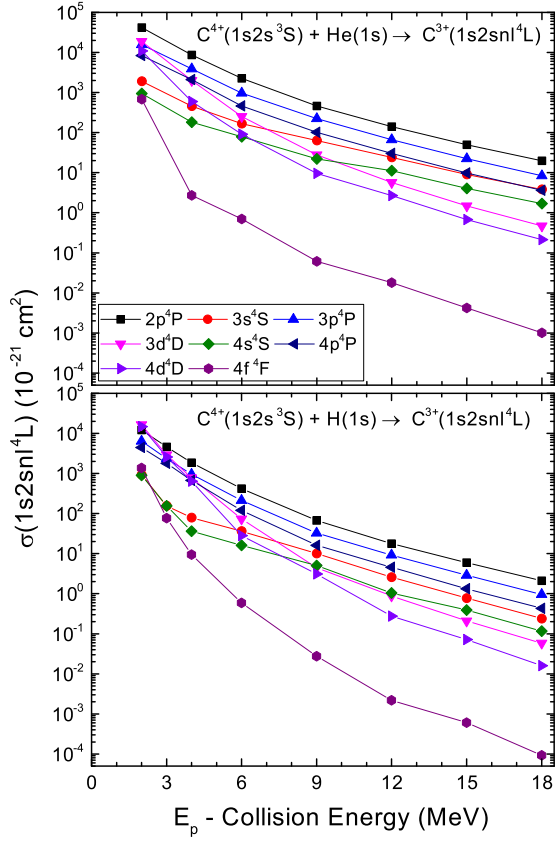


FIG. 6. Calculated total nl SEC cross sections for the production of the $1s2snl^4L$ states (for short nl^4L) for $n = 2, 3, 4$ levels in collisions of $C^{4+}(1s2s^3S)$ with one-electron targets: (top) He and (bottom) H (both as listed in Table VII).

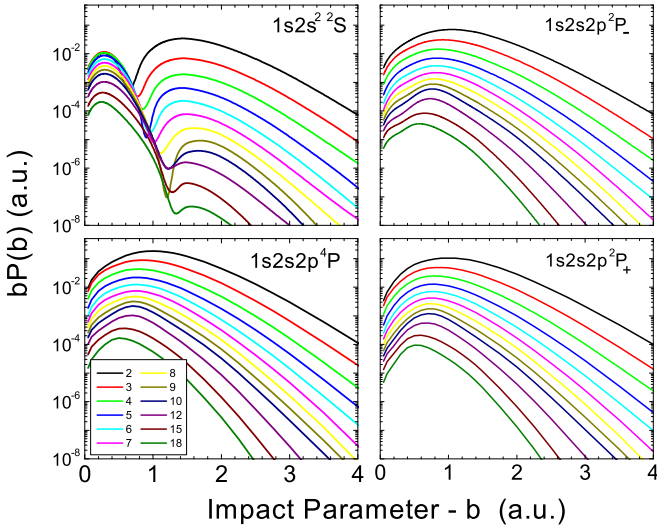


FIG. 7. 3eAOCC reduced probability $bP(b)$ impact parameter dependence for the production of the $1s2s^2^2S$, $1s2s2p^2P_-$, $1s2s2p^2P_+$, and $1s2s2p^4P$ states in collisions of $C^{4+}(1s2s^3S)$ ions with He targets. The lines from top to bottom at $b = 2$ a.u. correspond to projectile energies, E_p , from 2 to 18 MeV, as numbered in the legend.

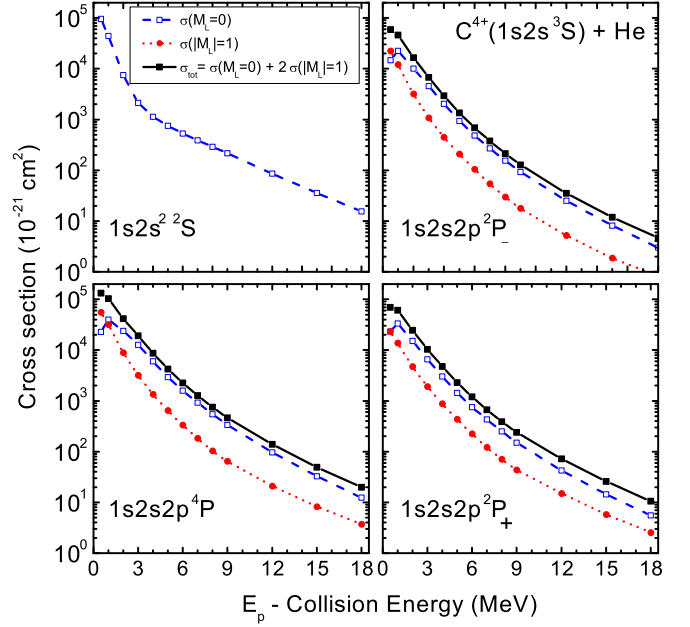


FIG. 8. 3eAOCC partial and total cross sections for the production of the $1s2s^2^2S$ ($L = 0$) and $1s2s2p^2P_-$, $1s2s2p^2P_+$, $1s2s2p^4P$ ($L = 1$) states in collisions of $C^{4+}(1s2s^3S) + \text{He}$ targets. Blue dashed line: partial cross section $\sigma(10)$ ($L = 1, M_L = 0$); red dotted line: partial cross section $\sigma(1|1|)$ ($L = 1, M_L = \pm 1$); black solid line: total cross section $\sigma_{\text{tot}}[1] = \sigma(1, 0) + 2\sigma(1|1|)$. Calculations as given in Tables V and VI for the doublets (2S , $^2P_{\pm}$) and 4P levels, respectively.

E. The ratios R and r

In Fig. 9 we show the ratio R of 4P to $^2P_{\pm}$ cross sections given by

$$R = \frac{\frac{1}{\xi[{}^4P]} \frac{d\sigma[{}^4P](0^\circ)}{d\Omega'}}{\frac{1}{\xi[{}^2P_-]} \frac{d\sigma[{}^2P_-](0^\circ)}{d\Omega'} + \frac{1}{\xi[{}^2P_+]} \frac{d\sigma[{}^2P_+](0^\circ)}{d\Omega'}}, \quad (37)$$

which after applying the Auger angular distributions Eqs. (35) and (36) is seen to be equivalent to the expression given in Ref. [28], i.e.,

$$R = \frac{\sigma[{}^4P](1, 0)}{\sigma[{}^2P_-](1, 0) + \sigma[{}^2P_+](1, 0)}, \quad (38)$$

with the explicit indication that the cross sections are evaluated for $M_L = 0$. Furthermore, $\sigma[{}^4P]$ includes (or not) the cascade contributions $\sigma_0^C[n \rightarrow \infty]$. Equation (37) is readily used to evaluate the experimental value of R , while its equivalent, Eq. (38), the theoretical value.

This ratio is shown for He and H_2 targets in Fig. 9 (bottom panel) as in Ref. [28], and here we present also the results for Ne and Ar (top panel). Figure 9 shows also the ratio $R = 2$ deduced from the frozen core approximation, inherently omitting cascade repopulation [18,28]. One can see an excellent agreement between the calculations including the cascade feeding of the 4P and the experimental data for the two targets He and H_2 (except at 6 MeV for the latter). The fact that the frozen core limit ($R = 2$) falls close to these results is therefore accidental. Comparing the results obtained for the four different targets, it is striking to see that the ratio

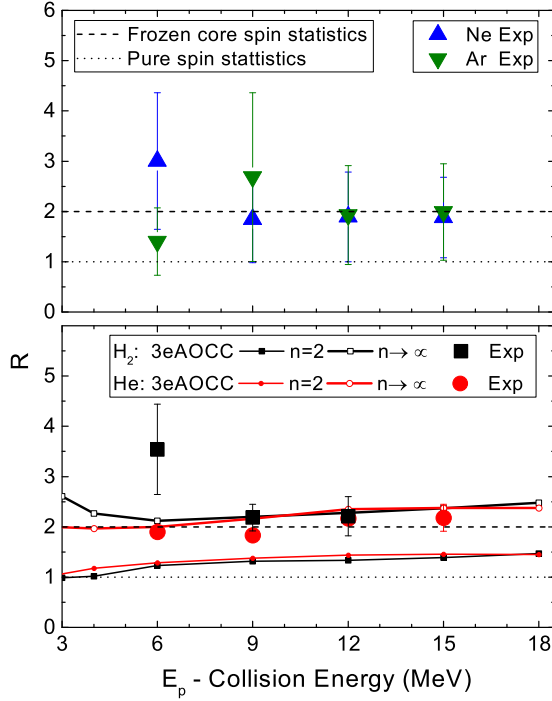


FIG. 9. Ratio R of 4P to the sum of $^2P_+$ and $^2P_-$ cross sections for $M_L = 0$, as given by Eq. (38) in collisions of $C^{4+}(1s2s^3S)$ ions with H_2 , He, Ne, and Ar targets. Lines marked $n \rightarrow \infty$ include also the cascade contributions to the 4P (see text). The values of R for He and H_2 have also appeared in Refs. [28,70]. (Bottom) Solid lines with symbols: 3eAOCC calculations, Symbols: measurements (red, He; black, H_2). (Top) Same as bottom, but only for experimental results for the Ne and Ar targets. The dashed lines correspond to the value for the frozen core spin statistics, while the dotted lines correspond to the value for the pure spin statistics. Only statistical uncertainties are shown. The error bars for Ne and Ar are larger than for He and H_2 since their determination necessarily include the additional error from the metastable fraction as demanded by the use of Eq. (11).

R follows a quite general tendency for high energies, above 9 MeV. This rather flat behavior clearly supports the Pauli shielding mechanism proposed in [28] and expected to be of a general nature.

In addition, we provide here further evidence for this finding by examining also the cross section ratio r of $^2P_+$ to $^2P_-$ similarly given by

$$r = \frac{\frac{1}{\xi[{}^2P_+]} \frac{d\sigma[{}^2P_+]}{d\Omega'}(0^\circ)}{\frac{1}{\xi[{}^2P_-]} \frac{d\sigma[{}^2P_-]}{d\Omega'}(0^\circ)} = \frac{\sigma[{}^2P_+](1,0)}{\sigma[{}^2P_-](1,0)} \quad (39)$$

with the explicit indication that the cross sections are evaluated for $M_L = 0$. In Fig. 10 (bottom), we compare 3eAOCC calculations of r to experimental 0° SDCS for He and H_2 . Considering only the spin statistics of the final $^2P_\pm$ states (pure spin statistics), r should have the value of 1 since both are doublets. However, assuming the frozen core approximation, and the recoupling scheme advocated in Ref. [29], r should have the value of 3. From Fig. 10 (bottom), it is evident that the values of r for both measurements and calculations lie in between these two limits, around the value of 2. The deviation of r from its pure statistical value of $r = 1$ can be

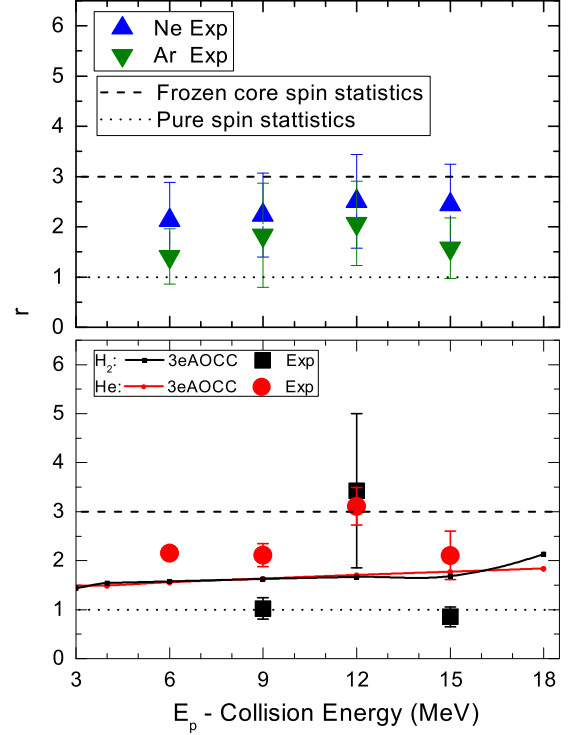


FIG. 10. Same as for Fig. 9, but for the ratio r of $^2P_+$ to $^2P_-$ cross sections for $M_L = 0$, as given by Eq. (39).

interpreted considering the Pauli shielding mechanism described in Ref. [28], using the Oppenheimer-Brinkman-Kramers (OBK) approximation. This first-order model (see the Supplemental Material in Ref. [28] for details) predicted that the transfer of the electron to the $C^{3+} 2p$ orbital to produce the 4P and $^2P_+$ is mainly driven by the attraction of the target electron by the carbon nucleus, while the production of $^2P_-$ involves only two-center electron-electron matrix elements, of smaller magnitude. Consequently, the $1s2s2p^2P_-$ cross section is inherently smaller than the ones corresponding to SEC to the $^2P_+$ state, with the ratio r being then larger than 1. This is in agreement with the results shown in Fig. 10, for He (bottom), as well as for Ar and Ne (top) targets, and partially for H_2 (bottom). Furthermore, this model predicted a value of $3/2$ for the ratio R , in agreement with our 3eAOCC calculations, as seen in Fig. 9 (bottom, $n = 2$ results, i.e., when not including cascade effects) and also Ref. [28].

One might expect that since the production of the two $1s2s2p^2P$ states proceeds by distinct mechanisms, this feature would also be reflected by different signatures in the impact parameter dependencies. However, no such effect is evident in Fig. 7, as the impact parameter dependence is similar for both states. The finding that the r values lie between the two limiting values of the pure spin statistics, and the frozen core spin statistics provides further support to the nonvalidity of spin statistics (pure or frozen core) in multielectron multiopen-shell dynamical atomic systems, first reported in [28].

F. Ar and Ne targets

The determination of the SDCS for the Ne and Ar heavy targets was performed according to Eq. (14). There the

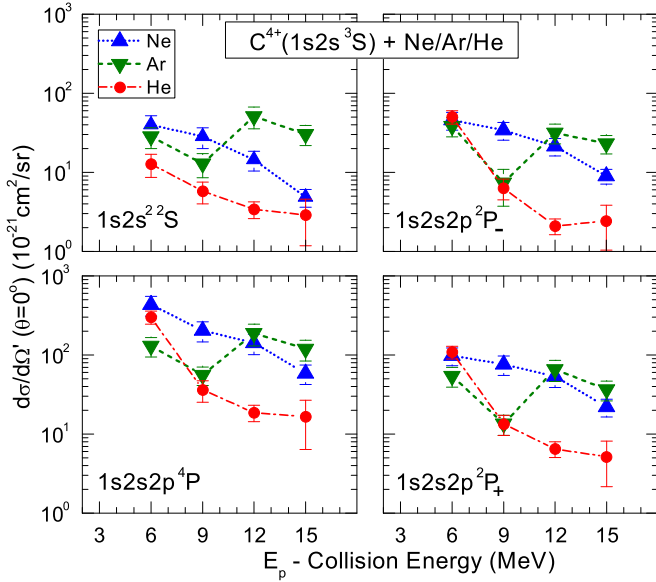


FIG. 11. Measured 0° Auger electron SDCS for the $1s2s^2S$, $1s2s2p^2P_-$, $1s2s2p^2P_+$, and $1s2s2p^4P$ states obtained in collisions of pre-excited $C^{4+}(1s2s^3S)$ beams with Ne and Ar targets. Corresponding results for He targets are also shown for comparison. Lines are drawn to guide the eye. Only statistical uncertainties are shown.

estimated average values of the metastable fractions, $f_{3S}^{[1]}$ and $f_{3S}^{[2]}$, were used for both measurements. Their 0° SDCS are shown in Fig. 11 in comparison to He. No theoretical attempt was made to model the heavy targets at present. It is seen that, for Ne targets, the cross section drops monotonically with increasing projectile energy, although not as rapidly as for the H_2 or He targets. This behavior clearly indicates that the SEC process with Ne resembles that of He and could therefore be possibly modeled in a similar way.

For Ar targets, the cross section is seen to be less sensitive to the dependence on the projectile energy, with a nonmonotonous behavior. Clearly this is inherently different from the Ne and He cases and may be due to the contribution of inner-valence electrons, certainly more likely for Ar than for Ne. This possibility should be further tested by theoretical calculations before validated.

Finally, the ratios R and r are also determined from the measured 0° SDCS for Ne and Ar and shown for comparison in Figs. 9 and 10. Similar values are seen for both Ne and Ar, as also found for He and H_2 , demonstrating the generality of the conclusions drawn in [28].

V. CONCLUSIONS

We report on a joint experimental and theoretical investigation of the fundamental process of single-electron capture in energetic collisions of pre-excited $C^{4+}(1s2s^3S)$ ions with gas targets. DDCSs for the production of the $C^{3+}(1s2snl^2,4L)$ states were determined with high-resolution for H_2 , He, Ne, and Ar gas targets, from which the corresponding SDCSs were obtained using our two-spectra measurement technique involving mixed-state $C^{4+}(1s^21S, 1s2s^3S)$ ion beams. Corresponding *ab initio* calculations based on a three active electrons atomic orbital close-coupling approach were performed for the H_2 and He targets resulting in an overall satisfactory agreement with experiment. The reduced probabilities $bP(b)$ as a function of the impact parameter b show a similar behavior for the P states, i.e., an increase followed by an exponential drop, while for the S state a minimum was observed. In addition, calculated partial cross sections clearly show that the main contribution to the total cross section comes from the $M_L = 0$ states, implying an alignment for the SEC process in the P states. The measured cross sections for the heavier Ne and Ar targets were not supported by calculations. However, the SDCSs for Ne targets are seen to have a similar projectile energy dependence as for He, while the Ar targets present a much different, rather constant, energy dependence within the experimental uncertainty. Finally, we provide further evidence, supported by measurements and calculations in fair agreement, for the nonvalidity of spin statistics population in multielectron multi-open-shell dynamical atomic systems, as reported in [28], by examining the ratio r of the doublet $^2P_+$ to $^2P_-$ cross sections, which is free of cascade repopulation. Further isoelectronic investigations involving other He-like projectiles are called for, with the same experimental and theoretical sophistication, to further probe the generality of these different findings.

ACKNOWLEDGMENTS

We would like to thank the personnel of the “Demokritos” Tandem for their help with the measurements. We acknowledge support by the project “Cluster of Accelerator Laboratories for Ion-Beam Research and Applications-CALIBRA” (MIS 5002799), which is implemented under the Action “Reinforcement of the Research and Innovation Infrastructure,” funded by the Operational Programme “Competitiveness, Entrepreneurship and Innovation” (NSRF 2014-2020) and cofinanced by Greece and the European Union (European Regional Development Fund).

- [1] C. T. Plowman, K. H. Spicer, I. B. Abdurakhmanov, A. S. Kadyrov, and I. Bray, Singly differential cross sections for direct scattering, electron capture, and ionization in proton-hydrogen collisions, *Phys. Rev. A* **102**, 052810 (2020).
- [2] J. W. Gao, Y. Wu, J. G. Wang, N. Sisourat, and A. Dubois, State-selective electron transfer in $He^+ + He$ collisions at intermediate energies, *Phys. Rev. A* **97**, 052709 (2018).

- [3] D. L. Guo, J. W. Gao, S. F. Zhang, X. L. Zhu, Y. Gao, D. M. Zhao, R. T. Zhang, Y. Wu, J. G. Wang, A. Dubois, and X. Ma, State-selective single-electron capture in intermediate-energy $C^{4+} + He$ collisions, *Phys. Rev. A* **103**, 032827 (2021).
- [4] S. Knoop, M. Keim, H. J. Lüdde, T. Kirchner, R. Morgenstern, and R. Hoekstra, State selective single-electron capture in $O^{6+} + Na$ collisions, *J. Phys. B: At. Mol. Opt. Phys.* **38**, 3163 (2005).

- [5] D. Röhrbein, T. Kirchner, and S. Fritzsche, Role of cascade and Auger effects in the enhanced population of the $C^{3+}(1s2s2p^4P)$ states following single-electron capture in $C^{4+}(1s2s^3S)$ -He collisions, *Phys. Rev. A* **81**, 042701 (2010).
- [6] L. F. Errea, B. Herrero, L. Mendez, and A. Riera, Molecular calculation of total and differential charge transfer cross sections in C^{4+} +He collisions, *J. Phys. B: At. Mol. Opt. Phys.* **28**, 693 (1995).
- [7] D. R. Schultz, M. R. Strayer, and J. C. Wells, Lattice, Time-Dependent Schrödinger Equation Solution for Ion-Atom Collisions, *Phys. Rev. Lett.* **82**, 3976 (1999).
- [8] D. L. Guo, X. Ma, R. T. Zhang, S. F. Zhang, X. L. Zhu, W. T. Feng, Y. Gao, B. Hai, M. Zhang, H. B. Wang, and Z. K. Huang, State-selective electron capture in 30- and 100-keVHe⁺+He collisions, *Phys. Rev. A* **95**, 012707 (2017).
- [9] A. B. Voitkiv and J. Ullrich, Three-body Coulomb dynamics in hydrogen ionization by protons and antiprotons at intermediate collision velocities, *Phys. Rev. A* **67**, 062703 (2003).
- [10] A. S. Schlachter, J. W. Stearns, W. G. Graham, K. H. Berkner, R. V. Pyle, and J. A. Tanis, Electron capture for fast highly charged ions in gas targets: An empirical scaling rule, *Phys. Rev. A* **27**, 3372 (1983).
- [11] M. Barat and P. Roncin, Multiple electron capture by highly charged ions at keV energies, *J. Phys. B: At. Mol. Opt. Phys.* **25**, 2205 (1992).
- [12] E. Y. Kamber, O. Abu-Haija, and J. A. Wardwell, State-selective electron capture by O^{3+} ions from atomic and molecular targets, *Phys. Rev. A* **77**, 012701 (2008).
- [13] D. Dijkkamp, A. Brazuk, A. G. Drentje, F. J. de Heer, and H. Winter, State-selective single-electron capture by 80 keV C^{4+} ions from He, H₂ and Li, *J. Phys. B* **16**, L343 (1983).
- [14] M. Trassinelli, C. Prigent, E. Lamour, F. Mezdari, J. Mérot, R. Reuschl, J.-P. Rozet, S. Steydli, and D. Vernhet, Investigation of slow collisions for (quasi) symmetric heavy systems: What can be extracted from high resolution x-ray spectra, *J. Phys. B: At. Mol. Opt. Phys.* **45**, 085202 (2012).
- [15] D. H. Lee, P. Richard, J. M. Sanders, T. J. M. Zouros, J. L. Shinpaugh, and S. L. Varghese, Electron capture and excitation studied by state-resolved KLL Auger measurement in 0.25–2 MeV/u $F^{7+}(1s^2^1S, 1s2s^3S)$ + H₂/He collisions, *Nucl. Instrum. Methods Phys. Res. B* **56–57**, 99 (1991).
- [16] J. A. Tanis, A. L. Landers, D. J. Pole, A. S. Alnaser, S. Hossain, and T. Kirchner, Evidence for Pauli Exchange Leading to Excited-State Enhancement in Electron Transfer, *Phys. Rev. Lett.* **92**, 133201 (2004).
- [17] D. Strohschein, D. Röhrbein, T. Kirchner, S. Fritzsche, J. Baran, and J. A. Tanis, Nonstatistical enhancement of the $1s2s2p^4P$ state in electron transfer in 0.5–1.0-MeV/u $C^{4,5+}$ +He and Ne collisions, *Phys. Rev. A* **77**, 022706 (2008).
- [18] T. J. M. Zouros, B. Sulik, L. Gulyás, and K. Tökési, Selective enhancement of $1s2s2p^4P_j$ metastable states populated by cascades in single-electron transfer collisions of $F^{7+}(1s^2/1s2s^3S)$ ions with He and H₂ targets, *Phys. Rev. A* **77**, 050701(R) (2008).
- [19] M. A. Abdallah, W. Wolff, H. E. Wolf, E. Y. Kamber, M. Stöckli, and C. L. Cocke, Single and double electron capture from He by Ar¹⁶⁺ studied using cold-target recoil-ion momentum spectroscopy, *Phys. Rev. A* **58**, 2911 (1998).
- [20] E. Y. Kamber, M. A. Abdallah, C. L. Cocke, and M. Stöckli, State-selective electron capture in (0.5–50)-keV/u C^{5+} – He collisions studied by cold-target recoil-ion momentum spectroscopy, *Phys. Rev. A* **60**, 2907 (1999).
- [21] D. Fischer, B. Feuerstein, R. D. DuBois, R. Moshhammer, J. R. C. Lopez-Urrutia, I. Draganic, H. Lorch, A. N. Perumal, and J. Ullrich, State-resolved measurements of single-electron capture in slow Ne⁷⁺- and Ne⁸⁺-helium collisions, *J. Phys. B* **35**, 1369 (2002).
- [22] S. Knoop, D. Fischer, Y. Xue, M. Zapukhlyak, C. J. Osborne, T. Ergler, T. Ferger, J. Braun, G. Brenner, H. Bruhns, C. Dimopoulou, S. W. Epp, A. J. G. Martínez, G. Sikler, R. S. Orts, H. Tawara, T. Kirchner, J. R. C. López-Urrutia, R. Moshhammer, J. Ullrich, et al., Single-electron capture in keV Ar^{15+...18+}+He collisions, *J. Phys. B: At. Mol. Opt. Phys.* **41**, 195203 (2008).
- [23] M. S. Schöffler, J. Titze, L. P. H. Schmidt, T. Jahnke, N. Neumann, O. Jagutzki, H. Schmidt-Böcking, R. Dörner, and I. Mančev, State-selective differential cross sections for single and double electron capture in He^{+,2+} – He and p – He collisions, *Phys. Rev. A* **79**, 064701 (2009).
- [24] D. L. Guo, X. Ma, S. F. Zhang, X. L. Zhu, W. T. Feng, R. T. Zhang, B. Li, H. P. Liu, S. C. Yan, P. J. Zhang, and Q. Wang, Angular- and state-selective differential cross sections for single-electron capture in p-He collisions at intermediate energies, *Phys. Rev. A* **86**, 052707 (2012).
- [25] P. Beiersdorfer, J. H. Scofield, and A. L. Osterheld, X-Ray-Line Diagnostic of Magnetic Field Strength for High-Temperature Plasmas, *Phys. Rev. Lett.* **90**, 235003 (2003).
- [26] T. R. Kallman and P. Palmeri, Atomic data for x-ray astrophysics, *Rev. Mod. Phys.* **79**, 79 (2007).
- [27] V. P. Shevelko and H. Tawara, editors, *Atomic Processes in Basic and Applied Physics* (Springer, Berlin, 2012)
- [28] I. Madesis, A. Laoutaris, T. J. M. Zouros, E. P. Benis, J. W. Gao, and A. Dubois, Pauli Shielding and Breakdown of Spin Statistics in Multielectron Multi-Open-Shell Dynamical Atomic Systems, *Phys. Rev. Lett.* **124**, 113401 (2020), and Supplemental Material.
- [29] E. P. Benis, T. J. M. Zouros, T. W. Gorczyca, A. D. González, and P. Richard, Elastic resonant and nonresonant differential scattering of quasifree electrons from B⁴⁺(1s) and B³⁺(1s²) ions, *Phys. Rev. A* **69**, 052718 (2004), Erratum, **73**, 029901(E) (2006)
- [30] J. W. Thomsen, J. Salgado, N. Andersen, D. Doweck, A. Dubois, J. C. Houver, S. E. Nielsen, and A. Svensson, Spatial dependence of electron transfer from optically prepared states: Li⁺+Na(3p) → Li(2p)+Na⁺, *J. Phys. B: At. Mol. Opt. Phys.* **32**, 5189 (1999).
- [31] I. D. Williams, J. Geddes, and H. B. Gilbody, Balmer α emission in collisions of H, H⁺, H₂⁺ and H₃⁺ with H₂, *J. Phys. B* **15**, 1377 (1982).
- [32] T. J. M. Zouros and D. H. Lee, Zero degree Auger electron spectroscopy of projectile ions, in *Accelerator-Based Atomic Physics: Techniques and Applications*, edited by S. M. Shafroth and J. C. Austin (AIP, Woodbury, NY, 1997), pp. 426–479.
- [33] S. Harissopoulos, M. Andrianis, M. Axiotis, A. Lagoyannis, A. G. Karydas, Z. Kotsina, A. Laoutaris, G. Apostolopoulos, A. Theodorou, T. J. M. Zouros, I. Madesis, and E. P. Benis, The Tandem Accelerator Laboratory of NCSR Demokritos: Current status and perspectives, *Eur. Phys. J. Plus* **136**, 617 (2021).
- [34] I. Madesis, A. Dimitriou, A. Laoutaris, A. Lagoyannis, M. Axiotis, T. Mertzimekis, M. Andrianis, S. Harissopoulos, E. P. Benis, B. Sulik, I. Valastyán, and T. J. M. Zouros, Atomic

- Physics with Accelerators: Projectile Electron Spectroscopy (APAPES), *J. Phys.: Conf. Ser.* **583**, 012014 (2015).
- [35] I. Madesis, A. Laoutaris, T. J. M. Zouros, S. Nanos, and E. P. Benis, Projectile electron spectroscopy and new answers to old questions: Latest results at the new atomic physics beamline in Demokritos, Athens, in *State-of-the-Art Reviews on Energetic Ion-Atom and Ion-Molecule Collisions*, Interdisciplinary Research on Particle Collisions and Quantitative Spectroscopy, Vol. 2, edited by D. Belkić, I. Bray, and A. Kadyrov (World Scientific, Singapore, 2019), pp. 1–31.
- [36] T. J. M. Zouros and E. P. Benis, The hemispherical deflector analyser revisited. I. Motion in the ideal $1/r$ potential, generalized entry conditions, Kepler orbits and spectrometer basic equation, *J. Electron Spectrosc. Relat. Phenom.* **125**, 221 (2002).
- [37] D. H. Lee, P. Richard, J. M. Sanders, T. J. M. Zouros, J. L. Shipaugh, and S. L. Varghese, KLL resonant transfer and excitation to $F^{6+}(1s2l2l')$ intermediate states, *Phys. Rev. A* **44**, 1636 (1991).
- [38] D. H. Lee, P. Richard, T. J. M. Zouros, J. M. Sanders, J. L. Shipaugh, and H. Hidmi, Binary encounter electrons observed at zero degrees in collisions of 1–2 MeV/amu H^+ , C^{6+} , N^{7+} , O^{8+} and F^{9+} , *Phys. Rev. A* **41**, 4816 (1990).
- [39] C. W. Woods, R. L. Kauffman, K. A. Jamison, N. Stolterfoht, and P. Richard, K-shell Auger-electron production cross sections from ion bombardment, *Phys. Rev. A* **13**, 1358 (1976).
- [40] E. P. Benis, I. Madesis, A. Laoutaris, S. Nanos, and T. J. M. Zouros, Mixed-state ionic beams: An effective tool for collision dynamics investigations, *Atoms* **6**, 66 (2018).
- [41] E. P. Benis and T. J. M. Zouros, Determination of the $1s2\ell 2\ell'$ state production ratios ${}^4P^o/{}^2P$, ${}^2D/{}^2P$ and ${}^2P_+/{}^2P_-$ from fast ($1s^2$, $1s2s^3S$) mixed-state He-like ion beams in collisions with H_2 targets, *J. Phys. B: At. Mol. Opt. Phys.* **49**, 235202 (2016).
- [42] M. Zamkov, H. Aliabadi, E. P. Benis, P. Richard, H. Tawara, and T. J. M. Zouros, Energy dependence of the metastable fraction in $B^{3+}(1s^2 1S, 1s2s^3S)$ beams produced in collisions with thin-foil and gas targets, *Phys. Rev. A* **64**, 052702 (2001).
- [43] M. Zamkov, H. Aliabadi, E. P. Benis, P. Richard, H. Tawara, and T. J. M. Zouros, Stripping energy dependence of $B^{3+}(1s2s^3S)$ beam metastable fraction, *AIP* **576**, 149 (2001).
- [44] E. P. Benis, M. Zamkov, P. Richard, and T. J. M. Zouros, Technique for the determination of the $1s2s^3S$ metastable fraction in two-electron ion beams, *Phys. Rev. A* **65**, 064701 (2002).
- [45] U. Schiebel, B. L. Doyle, J. R. Macdonald, and L. D. Ellsworth, Projectile K x rays from Si^{12+} ions in the $1s2s^3S_1$ metastable state incident on helium gas, *Phys. Rev. A* **16**, 1089 (1977).
- [46] M. Terasawa, T. J. Gray, S. Hagmann, J. Hall, J. Newcomb, P. Pepmiller, and P. Richard, Electron capture by and electron excitation of two-electron fluorine ions incident on helium, *Phys. Rev. A* **27**, 2868 (1983).
- [47] T. R. Dillingham, J. Newcomb, J. Hall, P. L. Pepmiller, and P. Richard, Projectile K-Auger-electron production by bare, one-, and two-electron ions, *Phys. Rev. A* **29**, 3029 (1984).
- [48] M. Zamkov, E. P. Benis, P. Richard, and T. J. M. Zouros, Fraction of metastable $1s2s^3S$ ions in fast He-like beams ($Z = 5-9$) produced in collisions with carbon foils, *Phys. Rev. A* **65**, 062706 (2002).
- [49] D. Schneider, R. Bruch, W. Butscher, and W. H. E. Schwarz, Prompt and time-delayed electron decay-in-flight spectra of gas-excited carbon ions, *Phys. Rev. A* **24**, 1223 (1981).
- [50] B. F. Davis and K. T. Chung, Complex-rotation method for spin-induced autoionization, *Phys. Rev. A* **36**, 1948 (1987).
- [51] E. P. Benis, S. Doukas, T. J. M. Zouros, P. Indelicato, F. Parente, C. Martins, J. P. Santos, and J. P. Marques, Evaluation of the effective solid angle of a hemispherical deflector analyser with injection lens for metastable Auger projectile states, *Nucl. Instrum. Methods Phys. Res. B* **365**, 457 (2015).
- [52] S. Doukas, I. Madesis, A. Dimitriou, A. Laoutaris, T. J. M. Zouros, and E. P. Benis, Determination of the solid angle and response function of a hemispherical spectrograph with injection lens for Auger electrons emitted from long lived projectile states, *Rev. Sci. Instrum.* **86**, 043111 (2015).
- [53] I. Madesis, Investigation of electron capture in swift $C^{4+}(1s2s^3S)$ collisions with gas targets using a zero-degree Auger projectile spectroscopy apparatus built with the L45 beam line at the “Demokritos” 5.5 MV tandem accelerator, Ph.D. thesis, University of Crete, Department of Physics, Heraklion, Greece, 2021.
- [54] M. H. Chen, B. Crasemann, and H. Mark, Deexcitation of light Li-like ions in the $1s2s2p$ state, *Phys. Rev. A* **27**, 544 (1983).
- [55] E. P. Benis, I. Madesis, A. Laoutaris, S. Nanos, and T. J. M. Zouros, Experimental determination of the effective solid angle of long-lived projectile states in zero-degree Auger projectile spectroscopy, *J. Electron Spectrosc. Relat. Phenom.* **222**, 31 (2018).
- [56] B. H. Bransden and M. R. C. McDowell, *Charge Exchange and the Theory of Ion-Atom Collisions* (Clarendon Press, Oxford, 1992).
- [57] Y. D. Wang, J. H. McGuire, and R. D. Rivarola, Impact-parameter treatment of high-velocity electron capture from diatomic molecules at fixed orientation, *Phys. Rev. A* **40**, 3673 (1989).
- [58] J. Caillat, N. Sisourat, A. Dubois, I. Sundvor, and J. P. Hansen, Orientation effects in $He^{2+}-H_2^+$ collisions at intermediate collision energies, *Phys. Rev. A* **73**, 014701 (2006).
- [59] N. Sisourat, I. Pilskog, and A. Dubois, Non perturbative treatment of multielectron processes in ion-molecule scattering: Application to $He^{2+}-H_2$ collisions, *Phys. Rev. A* **84**, 052722 (2011).
- [60] L. F. Shampine and M. K. Gordon, *Computer Solution of Ordinary Differential Equations: The Initial Value Problem* (W. H. Freeman, San Francisco, 1975).
- [61] L. Engstrom, P. Bengtsson, C. Jupen, and M. Westerlind, Extended analysis of the spectrum and term system of He-like carbon, *J. Phys. B: At. Mol. Opt. Phys.* **25**, 2459 (1992).
- [62] NIST Atomic Spectra Database for C V, https://physics.nist.gov/PhysRefData/ASD/levels_form.html.
- [63] P. D. Dumont, H. P. Garnir, Y. Baudinet-Robinet, and K. T. Chung, Quartet system of CIV, *Phys. Rev. A* **32**, 229 (1985).
- [64] W. Mehlhorn and K. Taulbjerg, Angular distribution of electrons from autoionising states with unresolved fine structure, *J. Phys. B* **13**, 445 (1980).
- [65] S. Fritzsche, A. Surzhykov, A. Gumberidze, and T. Stöhlker, Electron emission from highly charged ions: Signatures of magnetic interactions and retardation in strong fields, *New J. Phys.* **14**, 083018 (2012).

- [66] M. H. Chen, Effect of intermediate coupling on angular distribution of Auger electrons, *Phys. Rev. A* **45**, 1684 (1992).
- [67] N. M. Kabachnik, J. Tulkki, H. Aksela, and S. Ricz, Coherence and correlation in the anisotropy of Ne KL-LLL satellite Auger decay, *Phys. Rev. A* **49**, 4653 (1994).
- [68] M. Benhenni, S. M. Shafroth, J. K. Swenson, M. Schulz, J. P. Giese, H. Schöne, C. R. Vane, P. F. Dittner, and S. Datz, Angular distribution of Auger electrons emitted through the resonant transfer and excitation process following $O^{5+}+He$ collisions, *Phys. Rev. Lett.* **65**, 1849 (1990).
- [69] M. Benhenni, S. M. Shafroth, and J. K. Swenson, Alignment in fast ion-atom collisions, *Nucl. Instrum. Methods Phys. Res. B* **86**, 28 (1994).
- [70] T. J. M. Zouros, S. Nikolaou, I. Madesis, A. Laoutaris, S. Nanos, A. Dubois, and E. P. Benis, Radiative cascade repopulation of $1s2s2p^4P$ states formed by single electron capture in 2–18 MeV collisions of $C^{4+}(1s2s^3S)$ with He, *Atoms* **8**, 61 (2020).
- [71] S. M. Younger and W. L. Wiese, Theoretical simulation of beam-foil decay curves for resonance transitions of heavy ions, *Phys. Rev. A* **17**, 1944 (1978).
- [72] J. W. Cooper, Photoionization from outer atomic subshells. A model study, *Phys. Rev.* **128**, 681 (1962).
- [73] R. Della Picca, P. D. Fainstein, M. L. Martiarena, N. Sisourat, and A. Dubois, Cooper minima and Young-type interferences in photoionization of one-electron molecular ions, *Phys. Rev. A* **79**, 032702 (2009).